SCIENCE CHINA
Physics, Mechanics & Astronomy

•Article•

August 2021 Vol. 64 No. 8: 284711
https://doi.org/10.1007/s11433-021-1694-8

Multi-resolution technique integrated with smoothed particle element method (SPEM) for modeling fluid-structure interaction problems with free surfaces

Ting Long[1,2,3,4†], Zhilang Zhang[1,2,3†], and Moubin Liu[1,2,3*]

[1] *Beijing Innovation Center for Engineering Science and Advanced Technology (BIC-ESAT), College of Engineering, Peking University, Beijing 100871, China;*
[2] *State Key Laboratory for Turbulence and Complex Systems, Department of Mechanics and Engineering Science, Peking University, Beijing 100871, China;*
[3] *Institute of Ocean Research, Peking University, Beijing 100871, China;*
[4] *School of Mechanical Engineering, Guangxi University, Guangxi 530004, China*

Received January 5, 2021; accepted March 23, 2021; published online July 1, 2021

Free-surface flows, especially those associated with fluid-structure interactions (FSIs), pose challenging problems in numerical simulations. The authors of this work recently developed a smoothed particle element method (SPEM) to simulate FSIs. In this method, both the fluid and solid regions are initially modeled using a smoothed finite element method (S-FEM) in a Lagrangian frame, whereas the fluid regions undergoing large deformations are adaptively converted into particles and modeled with an improved smoothed particle hydrodynamics (SPH) method. This approach greatly improves computational accuracy and efficiency because of the advantages of the S-FEM in efficiently treating solid/fluid regions showing small deformations and the SPH method in effectively modeling moving interfaces. In this work, we further enhance the efficiency of the SPEM while effectively capturing local fluid information by introducing a multi-resolution technique to the SPEM and developing an effective approach to treat multi-resolution element-particle interfaces. Various numerical examples demonstrate that the multi-resolution SPEM can significantly reduce the computational cost relative to the original version with a constant resolution. Moreover, the novel approach is effective in modeling various incompressible flow problems involving FSIs.

smoothed particle element method (SPEM), smoothed finite element method (S-FEM), smoothed particle hydrodynamics (SPH), multi-resolution technique, fluid-structure interaction

PACS number(s): 02.70.-c, 46.15.-x, 47.11.-j, 83.50.-v

Citation: T. Long, Z. Zhang, and M. Liu, Multi-resolution technique integrated with smoothed particle element method (SPEM) for modeling fluid-structure interaction problems with free surfaces, Sci. China-Phys. Mech. Astron. **64**, 284711 (2021), https://doi.org/10.1007/s11433-021-1694-8

1 Introduction

Free-surface flows widely exist in numerous natural and industrial systems in which fluids usually interact with rigid and flexible structural subcomponents. Developing adequate mathematical models and simulation strategies for underlying fluid-structure interaction (FSI) mechanisms is an important subarea in the field of computational fluid dynamics (CFD) [1]. In this area, tedious problems arise because of the large deformations of solids and the large-scale motion of fluids, free surfaces, and moving fluid-structure interfaces. The inherent nonlinearity and time-dependent characteristics of these problems present great challenges in

*Corresponding author (email: mbliu@pku.edu.cn)
†These authors contributed equally to this work.

their numerical modeling. Hence, the demand for truly predictive computational methods in industries, medical fields, research laboratories, space exploration, and many other fields has grown.

To model the incompressible flows involving FSI problems, there are two main approaches relying on grid-based methods in a Lagrangian or Eulerian frame. The Lagrangian finite element method (FEM) cannot effectively simulate incompressible flows with large deformations (e.g., free-surface flows). In such cases, this method requires mesh adjustment or rezoning. Idelsohn et al. [2] pioneered the combination of the Lagrangian FEM with a particle-based method and developed the particle finite element method (PFEM) for modeling incompressible flows with free surfaces. In the PFEM, the equations of fluid motion are solved by the FEM in a Lagrangian description, and the mesh nodes are regarded as moving material points. Recently, the PFEM has been successfully coupled with the FEM for the simulation of FSI problems [3,4], in which the PFEM is utilized to solve fluid flows and the FEM is applied to model solid structures. Despite the successful applications of the PFEM, it requires overcoming mesh entanglements and may thus entail additional topological modifications and an overall volume variation [5].

As for modeling incompressible flows in an Eulerian frame, the FEM [6], finite volume method (FVM) [7], and finite difference method (FDM) [8] have been widely employed. In dealing with violent FSI problems, these methods may require special techniques, such as the volume of fluid (VOF) [9] and level set (LS) [10], to track changing interfaces or free surfaces. This requirement usually brings great difficulties in accurately reproducing breaking free surfaces. Moreover, some complicated mesh generation techniques are necessary in situations involving complex geometries or moving boundaries.

Meshfree and particle methods have special advantages in modeling incompressible flows with free surfaces because they can naturally capture moving interfaces. The smoothed particle hydrodynamics (SPH) method is a popular meshfree method that has been successfully applied to different fields of engineering and science, such as free-surface flows [11-13], multiphase flows [14-17], heat and mass transfer [18-20], explosion phenomenon [21,22], and others [23-25]. Some researchers have coupled the SPH method with other Lagrangian or Eulerian grid-based methods for treating incompressible flow problems. To take advantage of the Lagrangian FEM for accurately and efficiently modeling structural deformations, coupling methodologies of SPH with FEM have been developed to treat various FSI problems [26,27]. For example, Hermange et al. [28] developed a coupling method for the SPH method and FEM to model some hydroelastic and 3D hydroplaning problems and achieved good accuracy and stability. Zhang et al. [29] investigated the mechanism of sloshing mitigation that takes advantage of SPH-FEM coupling method for treating the FSI problem of violent sloshing with deformable baffles. Coupling strategies of SPH with FVM [30,31] and SPH with FDM [32] also have been successfully presented while leveraging the capabilities of Eulerian grid-based methods in treating wall regions or efficiently modeling flows in a large domain. However, the FEM-SPH coupling approach treats fluid regions by using SPH and is thus computationally expensive. The FVM/FDM-SPH coupling approaches still suffer from the drawbacks of grid-based methods in modeling breaking free surfaces, and they are not able to effectively solve FSI problems with large structural deformations.

The multi-resolution techniques have recently been developed for grid-based and particle-based methods. In cases with computational domains that are much larger than solid structures, the use of a uniform mesh or particle distribution is prohibitive in terms of computational costs. Therefore, some researchers have developed adaptive mesh refinement (AMR) [33,34] for grid-based methods and adaptive particle resolution (APR) [35,36] for particle-based methods. In this way, as local fluid regions are modeled using refined grids or particles, the computational accuracy for regions with fine resolution can be improved with greatly reduced central processing unit (CPU) time and memory consumption. For the SPH method, some researchers have attempted to use variable particle spacing to overcome the drawbacks of using uniform particle distributions. In recent years, a challenging approach to implement multi-resolution simulations in SPH has emerged, and it is based on particle splitting and coalescing techniques [35,37], or called adaptive particle resolution [36,38,39]. Feldman and Bonet [40] first developed a particle refinement technique in which a coarse particle is split into several children particles to increase the spatial resolution in local regions. As the major part of the computational domain is modeled using coarse particles, the approach can significantly reduce CPU time relative to simulations that use refined particles for the whole domain. López et al. [41] improved this technique by maintaining the conservation of the change rate of density during the refinement process. Furthermore, Vacondio et al. [35,42] presented a dynamic particle resolution approach by incorporating a coarsening technique in which children particles can coalesce back to mother particles. Barcarolo et al. [36] developed an APR technique where mother particles are not removed after splitting but switched off and are turned on after passing through the refinement region. Although the refinement region can be moving in many of these refinement techniques, the fixed configurations of the region (e.g., square region) are usually used to easily implement the multi-resolution technique, whereas arbitrarily shaped and varying refinement regions may be desirable in some practical simulations.

The smoothed finite element method (S-FEM) developed by Liu et al. [43] can solve the usual problem of "overly-stiff" in the conventional FEM. The S-FEM accurately models structural deformations and can greatly reduce the computational time for fluid modeling as compared to the particle-based methods. To take advantages of the S-FEM and SPH method, Zhang et al. [1] developed the smoothed element-particle method (SPEM) for modeling FSI problems. In this approach, fluid and structural regions are initially simulated using the Lagrangian S-FEM. During the simulation, the finite elements in local fluid regions under large deformations are adaptively converted into particles, while the other fluid regions without large deformations are still modeled using finite elements. In this way, computational efficiency is significantly improved relative to that of conventional particle-based methods, such as the SPH method. Meanwhile, free surfaces and moving interfaces can be effectively captured by particles. In recent years, multi-resolution simulations have become increasingly popular because they entail low computational costs and achieve high accuracy for local fluid regions (e.g., boundary layer regions). In the current work, we focus on developing a multi-resolution technique for the SPEM to further improve computational efficiency along with computational accuracy for local domains. With this newly developed technique, the multi-resolution element-particle interfaces are successfully treated by splitting ghost fluid particles, and the multi-resolution regions can be arbitrary and vary with FSI interfaces. The multi-resolution SPEM is expected to effectively treat various FSI problems with significantly reduced computation costs.

The remainder of this paper is organized as follows. The methodologies, including the Lagrangian S-FEM formulations and the improved SPH method, are introduced in sect. 2. The multi-resolution technique for the SPEM and the presented algorithms for treating multi-resolution element-particle interfaces are also described in detail. Four numerical examples are presented and elucidated in sect. 3 to show the accuracy and efficiency of the presented method. Finally, conclusions are summarized in sect. 4, along with some remarks.

2 Methodology development

In the first part of this section, the Lagrangian S-FEM formulations for fluid and solid modeling are derived. In the second part, the improved SPH benefiting from several advanced techniques is described. In the third part, we introduce the multi-resolution technique implemented in the SPEM and the multi-resolution interface treatment in detail. The coupling strategy for fluids and solids is also described.

2.1 Lagrangian S-FEM for fluids and solids

In the SPEM, both structural deformations and fluid flows are modeled by the edge-based S-FEM with an updated Lagrangian description [1]. Three-node triangular elements are employed to discretize the computational domain. In the current configuration, the spatial position and velocity are obtained by

$$\begin{cases} x^{\alpha} = N_I x_I^{\alpha}, \\ v^{\alpha} = N_I v_I^{\alpha}, \end{cases} \tag{1}$$

where α, N_I, x_I, and v_I denote the dimension index, shape function, current spatial position, and velocity of node I, respectively. In the S-FEM, smoothing domains are used to solve the smoothed gradient of the field (Figure 1). On the basis of the divergence theorem, the smoothed velocity gradient can be derived as:

$$\begin{cases} \bar{v}^{\alpha,\beta} = \dfrac{1}{A_k^{\mathrm{s}}}\displaystyle\int_{\Gamma_k^{\mathrm{s}}} v^{\alpha} n^{\beta} \mathrm{d}\Gamma = \frac{1}{A_k^{\mathrm{s}}}\int_{\Gamma_k^{\mathrm{s}}} N_I v_I^{\alpha} n^{\beta} \mathrm{d}\Gamma = \overline{\left(\frac{\partial N_I}{\partial x^{\beta}}\right)} v_I^{\alpha}, \\ \overline{\left(\dfrac{\partial N_I}{\partial x^{\beta}}\right)} = \dfrac{1}{A_k^{\mathrm{s}}}\displaystyle\int_{\Gamma_k^{\mathrm{s}}} N_I n^{\beta} \mathrm{d}\Gamma, \end{cases} \tag{2}$$

where A_k^{s} denotes the area of the smoothing domain Ω_k^{s} in a two-dimensional space, superscript "s" denotes the field variable of the solid, and n^{β} represents the component of the unit vector normal to the smoothing domain boundary Γ_k^{s}.

Using the principle of virtual power, we obtain the following equation:

$$\int_{\Omega} \delta \overline{\left(\frac{\partial v^{\alpha}}{\partial x^{\beta}}\right)} \bar{\sigma}^{\beta\alpha} \mathrm{d}\Omega - \int_{\Omega} \delta v^{\alpha} \rho b^{\alpha} \mathrm{d}\Omega - \int_{\Gamma_t} \delta v^{\alpha} \bar{T}^{\alpha} \mathrm{d}\Gamma + \int_{\Omega} \delta v^{\alpha} \rho a^{\alpha} \mathrm{d}\Omega = 0. \tag{3}$$

By further employing the shape function of polynomial interpolation, we rewrite eq. (3) as:

$$\int_{\Omega} \overline{\left(\frac{\partial N_I}{\partial x^{\beta}}\right)} \bar{\sigma}^{\beta\alpha} \mathrm{d}\Omega - \int_{\Omega} N_I \rho b^{\alpha} \mathrm{d}\Omega - \int_{\Gamma_t} N_I \bar{T}^{\alpha} \mathrm{d}\Gamma + \int_{\Omega} N_I \rho N_J a_J^{\alpha} \mathrm{d}\Omega = 0, \qquad \forall I \notin \Gamma_{\mathrm{v}}, \tag{4}$$

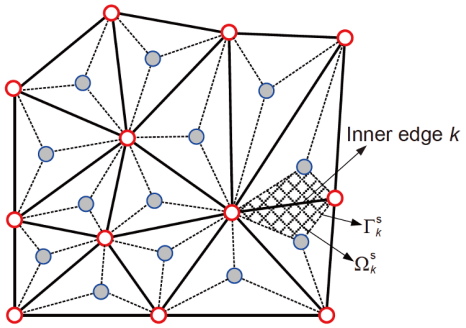

Figure 1 (Color online) Partition of smoothing domains (shaded areas) with triangular elements (solid lines).

where δv, $\overline{\sigma}$, ρ, a, $\overline{T}$, b, and Γ_v represent the virtual velocity, smoothed Cauchy stress, density, acceleration, surface force, body force, and boundary of velocity, respectively. Finally, the nonlinear solid deformations are calculated using the explicit time integration based on the central difference algorithm. The S-FEM formulas for structural deformations are

$$\begin{cases} M_I a_I^{\alpha} + f_{I\_\text{int}}^{\alpha} = f_{I\_\text{ext}}^{\alpha}, \\ f_{I\_\text{int}}^{\alpha} = \int_{\Omega} \overline{\left(\frac{\partial N_I}{\partial x^{\beta}}\right)} \overline{\sigma}^{\beta\alpha} \mathrm{d}\Omega, \\ f_{I\_\text{ext}}^{\alpha} = \int_{\Omega} N_I \rho b^{\alpha} \mathrm{d}\Omega + \int_{\Gamma_t} N_I \overline{T}^{\alpha} \mathrm{d}\Gamma, \end{cases} \tag{5}$$

where M_I is the node mass. The equivalent internal force f_{I_int} represents the contribution of Cauchy stress, and the equivalent external force f_{I_ext} represents the contribution of body and surface forces.

In the SPEM, the edge-based S-FEM in a Lagrangian frame is utilized to model incompressible flows. The relevant mathematical relations are presented here. The Cauchy stress tensor in the equations of fluid motion is written as:

$$\sigma^{\alpha\beta} = -p\delta^{\alpha\beta} + \tau^{\alpha\beta}, \tag{6}$$

where δ and τ represent the unit tensor and deviator stress, respectively. Similar to the weakly compressible SPH [23,24], an artificial equation of state is applied to compute pressure by regarding the incompressible fluid as weakly compressible, i.e.,

$$p = c^2(\rho - \rho_0), \tag{7}$$

where c and ρ_0 are the numerical sound speed and reference density, respectively. Sound speed is usually restricted by $c \geq 10\max(U_{\max}, \sqrt{p_{\max}/\rho_0})$ to satisfy the weakly compressible condition [44,45]. $U_{\max}$ and $p_{\max}$ respectively denote the maximum expected velocity and pressure of the fluid. Smoothed pressure $\overline{p}$ is constructed by the smoothed velocity gradient given as:

$$\frac{\mathrm{d}\overline{p}}{\mathrm{d}t} = -c^2\rho\overline{\left(\frac{\partial N_I}{\partial x^{\alpha}}\right)} v_I^{\alpha}. \tag{8}$$

The deviator strain rate ε and its smoothed value are written as:

$$\begin{cases} \varepsilon^{\alpha\beta} = \frac{1}{2}\left(\frac{\partial v^{\alpha}}{\partial x^{\beta}} + \frac{\partial v^{\beta}}{\partial x^{\alpha}}\right) - \frac{1}{3}\left\{\frac{\partial v^{\alpha}}{\partial x^{\alpha}}\right\}\delta^{\alpha\beta}, \\ \overline{\varepsilon}^{\alpha\beta} = \frac{1}{2}\left\{\overline{\left(\frac{\partial N_I}{\partial x^{\beta}}\right)} v_I^{\alpha} + \overline{\left(\frac{\partial N_I}{\partial x^{\alpha}}\right)} v_I^{\beta}\right\} - \frac{1}{3}\left\{\overline{\left(\frac{\partial N_I}{\partial x^{\alpha}}\right)} v_I^{\alpha}\right\}\delta^{\alpha\beta}. \end{cases} \tag{9}$$

Finally, the smoothed deviator stress and smoothed Cauchy stress are given by

$$\begin{cases} \overline{\tau}^{\alpha\beta} = 2\mu\overline{\varepsilon}^{\alpha\beta}, \\ \overline{\sigma}^{\alpha\beta} = -\overline{p}\,\delta^{\alpha\beta} + \overline{\tau}^{\alpha\beta}, \end{cases} \tag{10}$$

where μ is the dynamic viscosity of the fluid. In a recent study presented by the authors [1], the set of such Lagrangian S-FEM formulas for incompressible fluid flows is called the weakly compressible S-FEM.

2.2 Improved SPH for local fluid regions

In the SPEM, we use an improved SPH to model local fluid regions. The SPH formulations for incompressible fluid flows are presented as follows. In SPH, kernel and particle approximations are employed to discretize the governing partial differential equations. For the kernel approximation, we use the kernel function W to calculate the interaction forces between SPH particles. Hence, a field function $f(\mathbf{x})$ and its spatial derivative $\nabla f(\mathbf{x})$ at position $\mathbf{x}$ are given by

$$\langle f(\mathbf{x})\rangle = \int_{\Omega} f(\mathbf{x}')W(\mathbf{x}-\mathbf{x}', h)\mathrm{d}\mathbf{x}', \tag{11}$$

$$\langle \nabla f(\mathbf{x})\rangle = -\int_{\Omega} f(\mathbf{x}')\nabla W(\mathbf{x}-\mathbf{x}', h)\mathrm{d}\mathbf{x}', \tag{12}$$

where Ω denotes the spatial domain, $< >$ shows the SPH approximation, and h stands for the smoothing length. For the particle approximation, the field function and its derivatives can be obtained by taking the sum of all the neighboring particles of the interested particle, i.e.,

$$\langle f(\mathbf{x}_i)\rangle = \sum_{j=1}^{N} \frac{m_j}{\rho_j} f(\mathbf{x}_j)W(\mathbf{x}_j - \mathbf{x}_i), \tag{13}$$

$$\langle \nabla f(\mathrm{x}_i)\rangle = \sum_{j=1}^{N} \frac{m_j}{\rho_j} f(\mathrm{x}_j)\nabla_i W_{ij}, \tag{14}$$

where m_j is the mass, ρ_j is the density of particle j, and N represents the total number of its neighboring particles.

For incompressible viscous hydrodynamic problems, the governing continuity and Navier-Stokes (N-S) equations in a Lagrangian frame are given by

$$\begin{cases} \frac{\mathrm{d}\rho}{\mathrm{d}t} = -\rho\nabla\cdot\mathbf{v}, \\ \frac{\mathrm{d}\mathbf{v}}{\mathrm{d}t} = -\frac{1}{\rho}\nabla p + \frac{\mu}{\rho}\nabla^2\mathbf{v} + \mathbf{b}. \end{cases} \tag{15}$$

Applying the kernel and particle approximations to the above eq. (15), along with some transformations, yields the following SPH forms of the governing equations:

$$\begin{cases} \frac{\mathrm{d}\rho_i}{\mathrm{d}t} = \sum_{j=1}^{N} m_j \mathbf{v}_{ij}\cdot\nabla_i W_{ij}, \\ \frac{\mathrm{d}\mathbf{v}_i}{\mathrm{d}t} = -\sum_{j=1}^{N} m_j\left(\frac{p_i}{\rho_i^2} + \frac{p_j}{\rho_j^2}\right)\nabla_i W_{ij} \\ \qquad + \sum_{j=1}^{N} \frac{4m_j(\mu_i+\mu_j)\mathbf{x}_{ij}\cdot\nabla_i W_{ij}}{(\rho_i+\rho_j)^2(x_{ij}^2 + 0.01h^2)}\mathbf{v}_{ij} + \mathbf{b}, \end{cases} \tag{16}$$

where $\mathbf{v}_{ij} = \mathbf{v}_i - \mathbf{v}_j$ and $\mathbf{x}_{ij} = \mathbf{x}_i - \mathbf{x}_j$. In modeling incompressible flows using SPH, one approach is to calculate

the pressure through the Poisson equation (PPE) (see refs. [46,47] about PPE). This approach is called the incompressible SPH (ISPH) method [48-50]. Another method considers incompressible fluid as weakly compressible and employs an artificial equation of state to update fluid pressure, i.e., the weakly compressible SPH (WCSPH) method [23,24]. In the current work, we apply the WCSPH to treat incompressible flows and adopt the state (eq. (7)).

The conventional SPH method suffers from low accuracy as it cannot exactly approximate linear functions and even constants. To improve the accuracy of the SPH method, Liu et al. [23,51] developed the finite particle method (FPM) with second-order accuracy. Since the introduction of the FPM, it has been successfully applied to the modeling of different problems in various fields [19,52,53]. However, the FPM is time consuming and not very stable because matrix equations are involved in the simulations. Recently, the authors developed a decoupled FPM that does not need to solve the corrective matrix while maintains a relatively high accuracy [1], and this approach is used in the current multi-resolution SPEM. To ensure a uniform particle distribution and obtain a stable and accurate solution, we also consider the particle shifting technique (PST) [54,55] in the present method. This technique helps by re-distributing particles and adapting the field variables.

2.3 Multi-resolution SPEM

2.3.1 Multi-resolution technique for SPEM

Feldman and Bonet [40] firstly presented a particle refinement technique for SPH. In this technique, one coarse particle is split into several children particles to increase the particle resolution in the concerned fluid regions. During the particle refinement process, the conservation of mass, kinetic energy, and linear and angular momenta of particles should be maintained. After the refinement, the change in the density and velocity fields surrounding the refined particles should also be minimized. Further details about this method are available in ref. [40]. Motivated by this idea, we integrate the particle refinement technique with the SPEM to implement a multi-resolution simulation.

In the multi-resolution SPEM, the same group-based conversion method is used to identify the elements to be converted into particles [1,56]. The entire fluid domain is partitioned into different groups at the beginning of the computation. The length Δ_g of the group is taken as $\Delta_g = \lambda(2h_{\max})$, where λ is the dilation factor larger than 1.0 and $h_{\max}$ is the maximum smoothing length of the particles to be converted in this group. In this method, the minimum interior angle (MIA) algorithm is employed to determine whether an element should be converted. Specifically, if the minimum interior angle of an element reaches a limited small value (30° in present simulations), then such element is regarded as a distorted element. If one distorted element occurs in a group, all the elements in such group are converted into particles. Converting one element into one particle in an instant instead of converting a group of elements is inappropriate because converting only one particle is computationally uneconomical and the element-particle interface can be discontinuous. Further details about the group-based conversion algorithm are described in refs. [1,56].

Figure 2 shows the conversion of a group of elements into particles and the implementation of the multi-resolution technique in the SPEM. After identifying the groups of elements to be converted into particles, we generate fluid particles in these groups and ghost particles in the surrounding groups of the unconverted elements. Then, the generated fluid particles are split into three particles to increase the spatial resolution in local regions. It should be noticed that the coarse fluid particles can also be split into four or seven particles, as introduced in ref. [40]. We find that as the triangle elements are used in this work, splitting one particle into three particles on the basis of the triangle elements can yield stable and accurate simulations. Furthermore, the ghost particles are split to overcome the discontinuity problem between the refined particles and the coarse elements.

First, we introduce the conversion of elements into particles and the particle refinement process. As shown in Figure 3, the element OPQ is identified as a converting element, and a fluid particle M is generated at its barycenter. The position and velocity of the new particle are

$$\begin{cases} \mathbf{x}_M = \dfrac{m_O\mathbf{x}_O + m_P\mathbf{x}_P + m_Q\mathbf{x}_Q}{m_e}, \\ v_M = \dfrac{m_O v_O + m_P v_P + m_Q v_Q}{m_e}, \end{cases} \tag{17}$$

where m_O, m_P, and m_Q are the masses of the element nodes and m_e is the mass of the corresponding element OPQ. The mass and density of particle M are the same as those of the element

$$\begin{cases} m_M = m_e, \\ \rho_M = \rho_e, \end{cases} \tag{18}$$

where m_e and ρ_e are the mass and density of the element OPQ, respectively. Second, particle M is split into three particles in the corresponding triangle element. To maintain the uniform distribution of the refined particles and the conservation of the element properties, we locate the refined particles at the center of particle M and element nodes, that is

$$\mathbf{x}_i = \frac{\mathbf{x}_O + \mathbf{x}_M}{2}, \mathbf{x}_j = \frac{\mathbf{x}_P + \mathbf{x}_M}{2}, \mathbf{x}_k = \frac{\mathbf{x}_Q + \mathbf{x}_M}{2}, \tag{19}$$

where $\mathbf{x}_i$, $\mathbf{x}_j$, and $\mathbf{x}_k$ denote the positions of the refined particles. To guarantee mass conservation, the mass of the three particles remains equal to one-third that of the element. We

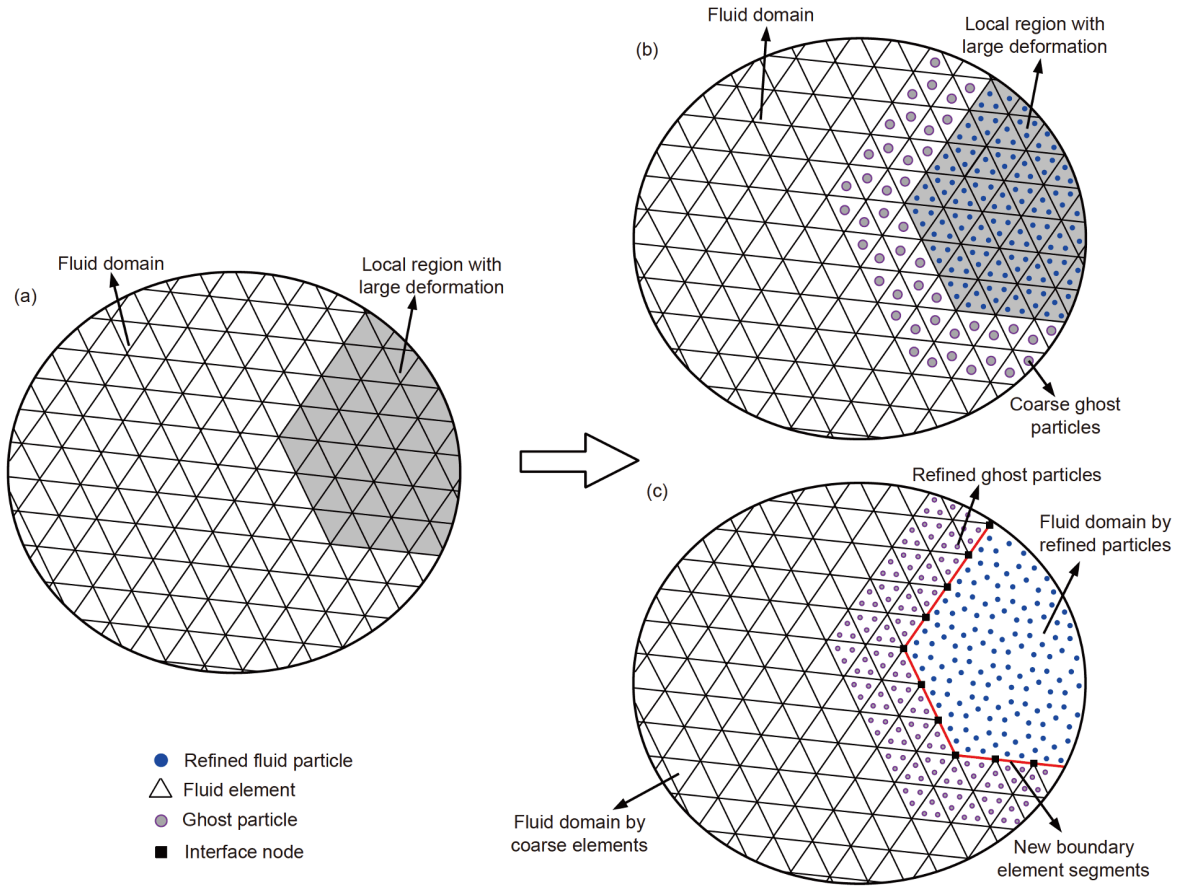

Figure 2 (Color online) Implementation of multi-resolution technique in SPEM, (a) determining the elements to be converted, (b) generating ghost and real fluid particles, (c) splitting the ghost/fluid particles and removing the local fluid elements.

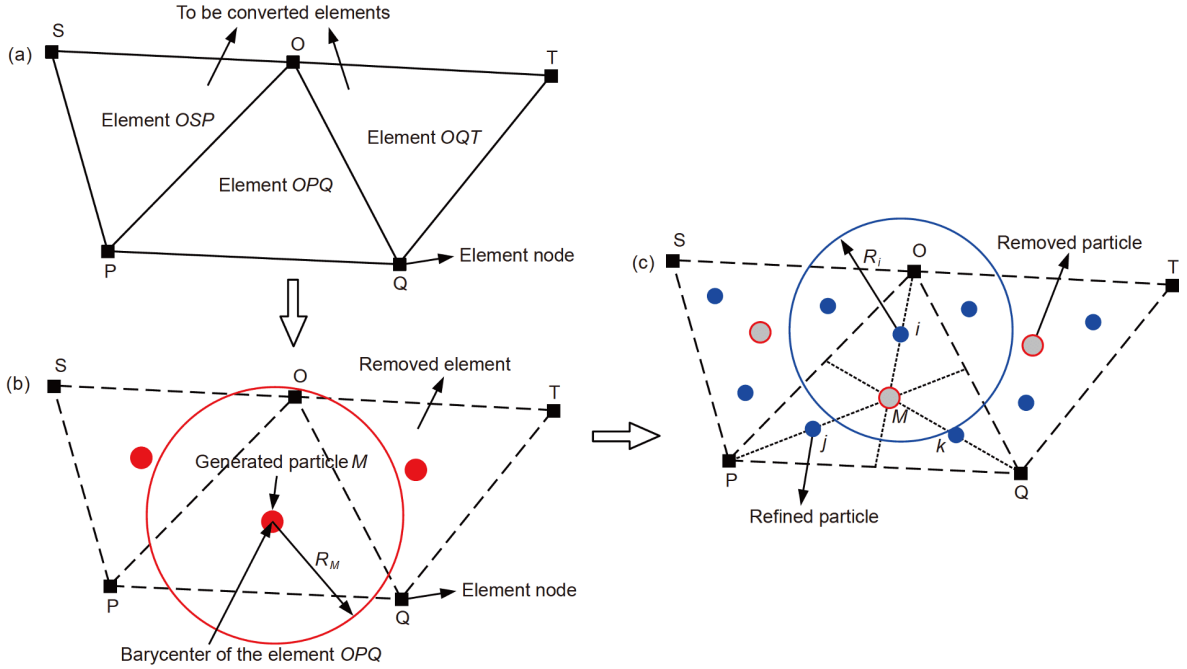

Figure 3 (Color online) Conversion of elements to particles. (a) Identification of converting elements; (b) generation of fluid particles; (c) refinement of fluid particles.

also set the density of the particles to be the same as that of the element; that is

$$\begin{cases} m_i = m_j = m_k = \dfrac{1}{3} m_e, \\ \rho_i = \rho_j = \rho_k = \rho_e. \end{cases} \tag{20}$$

Moreover, the momentum conservation is maintained, and the velocity of a refined particle is adopted as that of the neighboring element node:

$$v_i = v_O, v_j = v_P, v_k = v_Q. \tag{21}$$

The radius of the coarse particle M is taken as:

$$R_M = \sqrt{A_e} / 2, \tag{22}$$

where A_e denotes the area of the triangular element. The radius of the refined particles $R_i = R_j = R_k$, and this value can be adopted as 0.5-0.6R_M. Using this approach, we can conserve the mass and momentum during the element-particle conversion and particle refinement processes.

After generating the refined particles, the boundary segments should be updated, as shown in Figure 2(c). The groups of refined particles are added into the list of fluid particles. The smoothing domain should also be reconstructed, as introduced in ref. [1]. Furthermore, the coupling strategy based on splitting ghost particles is presented to calculate the interaction forces between the fluid elements and the fluid particles. The coupling in the conventional SPEM involves locating one ghost particle in each element of the interface regions, and such ghost particle carries the information of the corresponding fluid element. Fluid particles are updated by considering the ghost particles as the neighboring particles in the computations of governing equations. The force on the element node is computed on the basis of the neighboring fluid particles. However, the sizes of the elements and particles are not consistent in the multi-resolution SPEM, and the relevant field variables, such as the mass or volume between the elements and particles, are not continuous. This condition may lead to computational errors in the interface regions. For instance, when particles are distributed nonuniformly, the support domain of one fluid particle may include a very small number of ghost particles due to the large size of the element (one ghost particle in each element). To calculate the interaction forces and solve the discontinuity problem, we split the ghost particles in the unconverted elements. As shown in Figure 4, the local fluid domain is modeled using refined particles while the other region is treated by coarse elements. We first detect the new boundary element segments of the element region and identify the surrounding groups of the particle region. Then, each of the ghost particles in these surrounding groups is split into three particles. The refined ghost particles carrying the information of the corresponding elements are obtained using the same approach as that used for the real fluid particles, i.e., eqs. (17) to (22). Furthermore, the force applied from the elements to the particles can be calculated using the splitting ghost particles. This force is obtained by including the ghost particles in the summations of the real fluid particle i, that is

$$\begin{cases} \left|\dfrac{\mathrm{d}\rho_i}{\mathrm{d}t}\right|_{\text{ghost}} = \rho_i \sum\limits_{k=1}^{N_{\text{sg}}} \dfrac{m_k}{\rho_k} v_{ik} \cdot \nabla_i W_{ik}, \\ \left|\dfrac{\mathrm{d}v_i}{\mathrm{d}t}\right|_{\text{ghost}} = -\sum\limits_{k=1}^{N_{\text{sg}}} m_k \left(\dfrac{p_i}{\rho_i^2} + \dfrac{p_k}{\rho_k^2}\right) \nabla_i W \\ \qquad\qquad + \sum\limits_{k=1}^{N_{\text{sg}}} \dfrac{4 m_k (\mu_i + \mu_k) x_{ik} \cdot \nabla_i W_{ik}}{(\rho_i + \rho_k)^2 (x_{ik}^2 + \eta^2)} v_{ik}, \end{cases} \tag{23}$$

where N_{sg} denotes the number of splitting ghost particles in the support domain of particle i. The total information of fluid particle i is finally updated by

$$\begin{cases} \left|\dfrac{\mathrm{d}\rho_i}{\mathrm{d}t}\right|_{\text{total}} = \left|\dfrac{\mathrm{d}\rho_i}{\mathrm{d}t}\right|_{\text{ghost}} + \left|\dfrac{\mathrm{d}\rho_i}{\mathrm{d}t}\right|_{\text{real}}, \\ \left|\dfrac{\mathrm{d}v_i}{\mathrm{d}t}\right|_{\text{total}} = \left|\dfrac{\mathrm{d}v_i}{\mathrm{d}t}\right|_{\text{ghost}} + \left|\dfrac{\mathrm{d}v_i}{\mathrm{d}t}\right|_{\text{real}}, \end{cases} \tag{24}$$

where $||_{\text{real}}$ represents the information obtained by the surrounding real fluid particles. This calculation follows the same approach (using eq. (16)) as that for the inner fluid particles. As the splitting ghost particles carry similar variables as the real fluid particles, including the mass, velocity, volume, and density, the information of the fluid particles is consequently updated using the continuous field variables.

At this point, we calculate the forces applied to the coarse elements; the calculation is similar to that in ref. [1]. Taking one interfacial element as an example, the interaction force from the particles to the segment PQ, F^{α}_{FtPQ}, can be obtained according to the stress of the surrounding fluid particles,

$$\begin{cases} F^{\alpha}_{FtPQ} = \dfrac{l_{PQ}\left(\sigma_Q^{\alpha\beta} + \sigma_P^{\alpha\beta}\right) n^{\beta}}{2}, \\ \sigma_Q^{\alpha\beta} = \dfrac{\sum\limits_{j=1}^{N_f} \dfrac{m_j}{\rho_j} \sigma_j^{\alpha\beta} W_{Qj}}{\sum\limits_{j=1}^{N_f} \dfrac{m_j}{\rho_j} W_{Qj}}, \end{cases} \tag{25}$$

where $\sigma_Q^{\alpha\beta}$ represents the Cauchy stress of the interface node Q and N_f is the number of neighboring fluid particles of this node. l_{PQ} and n^{β} denote the segment length and unit vector normal to PQ, respectively. Finally, $F^{\alpha}_{FtPQ}/2$ is applied on both the nodes of P and Q. Furthermore, the velocity of the interface node is corrected by

$$\mathbf{v}_i^{Intf\_\text{node}} = \mathbf{v}_i^{Intf\_\text{node}} - \varphi \sum_j \frac{m_j}{\rho_j} (\mathbf{v}_i^{Intf\_\text{node}} - \mathbf{v}_j) W_{ij}, \tag{26}$$

where φ is a manually adjusted parameter and is adopted as

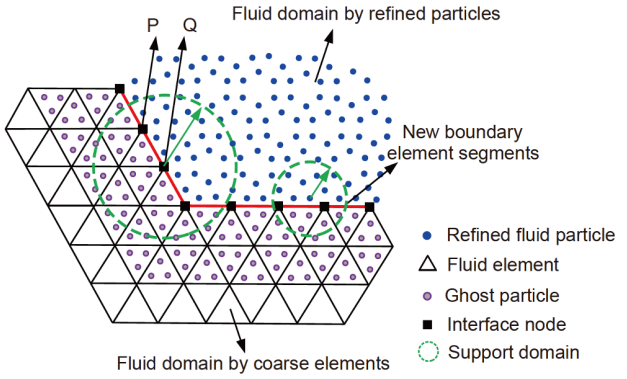

Figure 4 (Color online) Coupling of refined particles with coarse elements based on splitting ghost particles.

0.1 in our present simulations. This approach makes the interface elements and particles move in a homologous manner.

In the multi-resolution simulations, the fluid region is calculated using aforementioned PST [54,55]. The PST helps obtain a uniform distribution for the refined particles and thus achieves stable and accurate calculation results. In this work, we only present an example of splitting one particle into three particles on the basis of the triangle elements in multi-resolution SPEM. Other particle refinement techniques with smaller refinement errors can be developed and integrated into the SPEM in the future.

2.3.2 *Coupling of structural elements and fluid particles*

As far as the simulations of FSI problems are concerned, the treatment of FSI interfaces is important as it directly influences computational accuracy. In the present work, we adopt the virtual particle coupling strategy [57] in the decoupled FPM scheme to transfer the information between the structural elements and the fluid particles [1]. This coupling strategy is different from the element-particle coupling algorithm in the previous section in which the field variables are continuous around the interfaces of the fluid elements and fluid particles. In the fluid-structure coupling strategy, the truncation region of the fluid particle is partitioned into different subregions to generate ghost particles. The element-particle interaction forces are exerted by these ghost particles. At this point, we need to detect the type of interaction between a fluid particle and an element segment. Different position relationships between the particle and the element segment should be recorded, i.e., the particle interacting with segment AB or BC shown in Figure 5.

As shown in Figure 5(b), the truncation area of particle i is partitioned into three subareas, namely, Ω_1, Ω_2, and Ω_3. The subareas are divided into small triangles and arches with ghost particles located at the centers. The information of a ghost particle is obtained from the neighboring fluid particles [57]. Then, the force applied to fluid particle i from the segment BC is given by

$$\begin{aligned}\mathbf{F}_{S_{BC}tF_i} &= \sum_{j\in\Omega_{BCMN}} \mathbf{F}_{G_jtF_i} \\ &= m_i\Bigg[-\sum_{j\in\Omega_{BCMN}} m_j\left(\frac{p_i}{\rho_i^2}+\frac{p_j}{\rho_j^2}\right)\nabla_i W_{ij} \\ &\quad + \sum_{j\in\Omega_{BCMN}} \frac{4m_j(\mu_i+\mu_j)\mathbf{x}_{ij}\cdot\nabla_i W_{ij}}{(\rho_i+\rho_j)^2(\mathbf{x}_{ij}^2+\eta^2)}\mathbf{v}_{ij}\Bigg],\end{aligned} \tag{27}$$

where $\mathbf{F}_{G_jtF_i}$ is the force applied to fluid particle i from ghost particle j. The boundary force from fluid particle i on segment BC is written as $\mathbf{F}_{F_itS_{BC}} = -\mathbf{F}_{S_{BC}tF_i}$. To restore consistency, we utilize the highly accurate approximation scheme in the coupling strategy. With this approach, we attain the variables of both fluid and ghost particles. Ref. [1] presents further details about this coupling strategy for treating FSI interfaces.

The present method can also be easily extended to the modeling of FSI problems with thin-walled structures. In the multi-resolution SPEM, we employ the S-FEM to describe structural deformations; this approach is suitable for modeling thin-walled structures, as shown in refs. [58,59]. Moreover, the present method shows promise in the modeling of FSI problems with the dynamic plastic response of plates when appropriate plastic deformation criteria are introduced [60].

2.3.3 *Extension of multi-resolution technique to 3D*

Herein, we show the extension of the present multi-resolution technique to 3D problems, as targeted for our future work. In ref. [1], the conversion of elements into particles in a 3D space was discussed in detail, i.e., the computational domain is partitioned into different cubes, and the group-based conversion algorithm is applied to the tetrahedron elements under large deformations. After converting the groups of elements, the generated fluid particles are split into four particles to increase the spatial resolution in local 3D regions. Similarly, the mother particles can be split into eight or more children particles. It is found that stable and accurate simulations can be obtained when splitting one particle into four children particles on the basis of tetrahedron elements. As shown in Figure 6, mother particle M is located at the barycenter of tetrahedron element $OPQR$ and is given the same mass and density as those of the corresponding element. The children/refined particles are generated at the center of the mother particle and the four element nodes in 3D. The density of the four children particles is the same as that of the tetrahedron element, and the mass of the children particles is adopted as one-fourth of that of the element so that the mass conservation can be maintained. To ensure momentum conservation, we keep the velocity of a refined particle equal to that of the neighboring element node. After

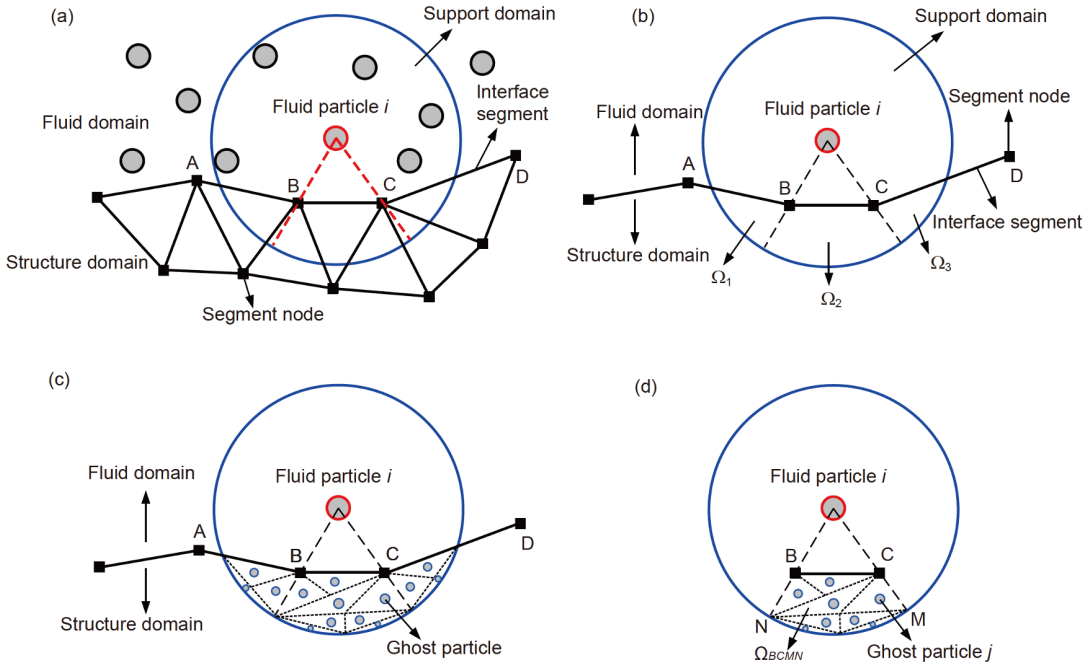

Figure 5 (Color online) Illustration of virtual particle strategy for treating FSI interfaces.

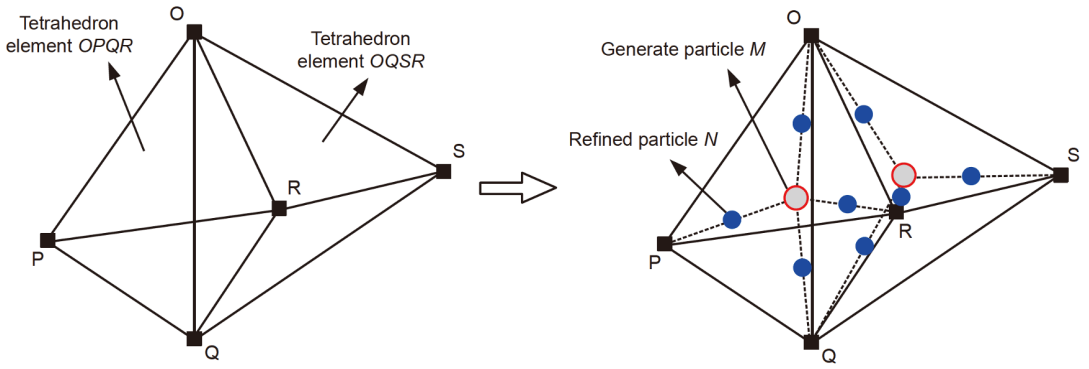

Figure 6 (Color online) Particle refinement process in 3D multi-resolution SPEM.

the provision of information to the four children particles, the boundary segments and smoothing domains in the 3D space can be updated using the same way as that introduced in ref. [1]. Another key point of the 3D multi-resolution technique is to couple the tetrahedron elements with the refined particles. This coupling can be achieved by splitting the ghost particles in unconverted elements and giving the ghost particles information in a way similar to that for real fluid particles. Furthermore, the variables of the refined fluid particles can be updated by regarding the split ghost particles as the neighborhood. The interaction forces applied to the element segments are computed according to the method introduced for 2D simulation. When extending the multi-resolution SPEM from 2D to 3D, the computational cost does not significantly increase. In the present coupling strategy, we only need to generate ghost particles for the fluid particles around the element-particle interfaces, i.e., a small number of ghost particles are generated for the limited fluid particles. Therefore, the element-particle coupling strategy in multi-resolution scheme additionally consumes very little computation time relative to that used in the entire simulation.

2.4 Differences between present multi-resolution technique and existing ones

In this section, we compare the present multi-resolution technique with existing ones in the context of SPH to illustrate the key point of our method. APR techniques [35,36] are known to show some advantages in modeling FSIs, but they need further development to become as mature as AMR techniques in grid-based methods [61]. One challenge is to maintain the mass, momentum, and energy conservation of the particle system during the particle splitting and coar-

sening processes that may affect the simulation accuracy and stability. Therefore, the position of the target region with a refined resolution is often determined in the computational domain [40] so that the particle splitting and coarsening technique can be easily and accurately implemented. A number of researchers have successfully moved the position of the refinement region in their simulations [35], and the same is done in our multi-resolution technique. More important, the multi-resolution regions in our method can be arbitrary and vary with FSI interfaces, and such interfaces should be identified during the simulation process. As shown in the water entry case in sect. 3.2, a rectangular region with refined particles (much smaller than the solid structure) is initially set around the water entry area. During the water entry process, the configuration of the refined region changes with the evolution of the fluid-structure interfaces. In the reported multi-resolution simulations of SPH, the moving refined region with a fixed configuration should be much larger than the solid structure, or the solid structure should be contained in the refined region. The adaptive refined region with configurations varying with the fluid-structure interfaces can be more efficient than conventional ones with large regions containing solid structures. The present adaptive multi-resolution technique provides a new alternative for researchers to implement multi-resolution simulations of FSI problems using SPH.

As mentioned previously, the configuration of the refinement region is usually fixed with regular interfaces between coarse and refined particles that need to be treated in the existing multi-resolution SPH. The overlapping particle region can be used to transfer information between coarse and fine particles (or named mother and children particles). Meanwhile, the artificially defined function can also be applied to transfer the field variables continuously. However, the multi-resolution interfaces in our developed algorithms become changing element-particle interfaces. The field variables should be accurately transferred from coarse elements to refined particles, as shown in Figure 4. This coupling is more challenging than the easy coupling of coarse particles with refined particles. Through the use of the proposed coupling algorithm based on splitting ghost particles, the field variables can be smoothly and continuously transferred between the coarse elements and the refined particles. The process is demonstrated in the following numerical tests. To the best of the authors' knowledge, the introduction of a multi-resolution technique to element-particle coupling approaches is rarely reported.

In summary, the present multi-resolution SPEM is very different from existing multi-resolution techniques adopted in particle-based methods. Specifically, the proposed method can treat moving multi-resolution regions with arbitrary shapes along with evolving FSI interfaces. The proposed algorithm for treating multi-resolution element-particle interfaces (rather than particle-particle interfaces) can also benefit the implementation of multi-resolution techniques in the coupling strategy of particle-based with grid-based methods, especially the SPH-FEM coupling approach.

3 Numerical tests

In this section, different examples are tested to show the accuracy and efficiency of the presented multi-resolution SPEM. First, a hydrostatic water column on an elastic plate is simulated to validate the accuracy of the multi-resolution element-particle interface treatment and show the convergence of the multi-resolution SPEM. Second, the water entry and exit cases are tested to validate the accuracy of our method and show its improved efficiency. Furthermore, the multi-resolution SPEM is applied to model a fluid-elastic structure interaction problem. The accuracy of the present method for treating FSI problems is demonstrated herein.

3.1 Hydrostatic water column on an elastic plate

In this section, we simulate the example of a hydrostatic water column on an elastic plate to investigate the consistency of the field variables across the multi-resolution element-particle interface. The model set-up of this case is similar to that shown in ref. [1]. The height and width of the still water column are $H = 2.0$ m and $L = 1.0$ m, respectively. The density of the fluid is $\rho = 1000$ kg/m^3, and the numerical sound speed is taken as $c = 100$ m/s. The elastic plate is set with a thickness of $e = 0.05$ m and a density of $\rho_s = 2700$ kg/m^3. The plate deformation is simulated by a linear elastic constitutive model with Young's modulus $E = 67.5$ GPa and Poisson's ratio $\upsilon = 0.34$. Except for specifically mentioned instants (e.g., water entry and exit in sect. 3.3), the acceleration of gravity is $g = 9.81$ m/s^2 in the present simulations.

Figure 7 shows the pressure distribution in the fluid and stress field in the solid plate obtained using the multi-resolution SPEM. The water column is discretized by both elements and particles, i.e., the height of the particle domain is 0.5 m. In this case, two coarse element distributions are adopted with element leg lengths $\Delta x_e = L/40$ and $L/60$. The refined particles are distributed by presetting the elements in the particle region and replacing each element with three particles. The solid plate is discretized with the same coarse resolution as the fluid element region. Figure 7 shows that the present method can attain a continuous pressure distribution across the multi-resolution element-particle interface. A smooth stress field is reproduced in the solid plate at the same time.

Moreover, we compare the midpoint displacements of the elastic plate computed through the multi-resolution SPEM

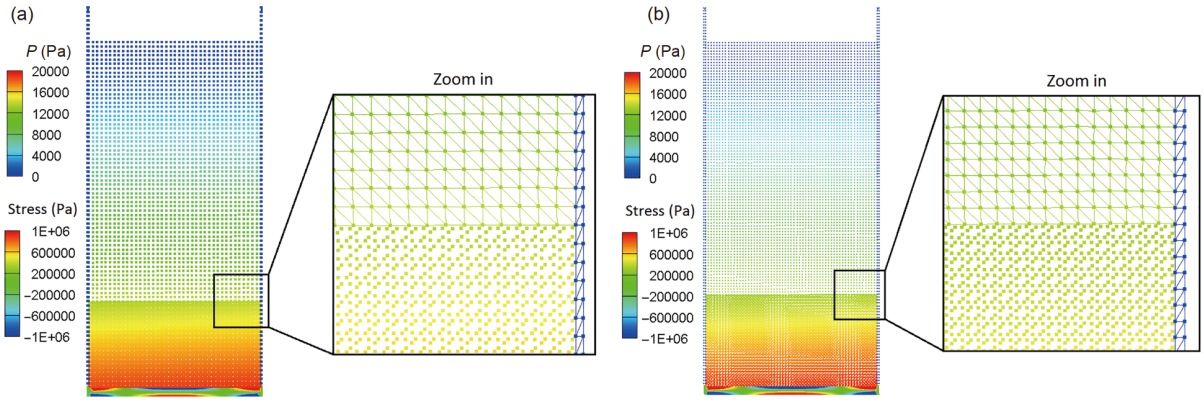

Figure 7 (Color online) Pressure distribution in fluid and stress field in solid plate obtained using multi-resolution SPEM, element leg lengths $\Delta x_e = L/40$ (a) and $L/60$ (b).

simulation and analytical solution (Figure 8). Three different coarse element lengths are considered, and the distribution of the refined particles is the same as that shown in Figure 7. The comparison indicates that with an increase in the spatial resolutions of the fluid and solid, the results of the multi-resolution SPEM approach the analytical ones. This test case demonstrates the accuracy of the multi-resolution SPEM in treating multi-resolution element-particle interfaces and the good convergence of the method.

3.2 Water entry of a wedge

In this section, the water entry of a wedge is simulated to validate the accuracy of the multi-resolution SPEM and demonstrate its efficiency. Figure 9 shows the schematic for the model set-up of this problem, which was also used by Oger et al. [62]. Zhao et al. [63] conducted an experiment for such a problem in which a wedge prism is freely released and impacts the water surface. Hence, this problem can be simplified as a 2D case. In this test, the width of the wedge is W = 0.5 m, and the dead rise angle of the wedge is 30°. Five piezoresistive pressure cells (P1-P5 in Figure 9) are used to record the wall pressure during the water entry process. Two force transducers are placed to test the vertical force on the falling wedge. The vertical velocity of the wedge is measured with an optical sensor. At T = 0 s, the wedge enters the water surface with a vertical velocity of 6.15 m/s. The density of water is $\rho_f = 1000$ kg/m^3. The length and depth of the computational fluid domain are set as 3.0 and 1.5 m, respectively. The numerical sound speed is taken as c = 100 m/s. A constant time step of 0.4×10^{-6} s is adopted for the present simulations. As shown in Figure 10, two different mesh distributions are used to test the accuracy and efficiency of the different approaches, respectively. In case I, the variable mesh size is used with a fine mesh distribution around the water entry region, i.e., the mesh size becomes smaller from the side and bottom walls to the water entry point. In case II, a fixed mesh size is employed for the entire computational domain.

The spatial resolution of the water entry region in case I is higher than that in case II and this keeps the higher accuracy of the simulation in case I. Hence, we first adopt case I to demonstrate the accuracy of the implementation of multi-resolution technique in SPEM. In case I, the computational domain is initially discretized using around 120000 elements

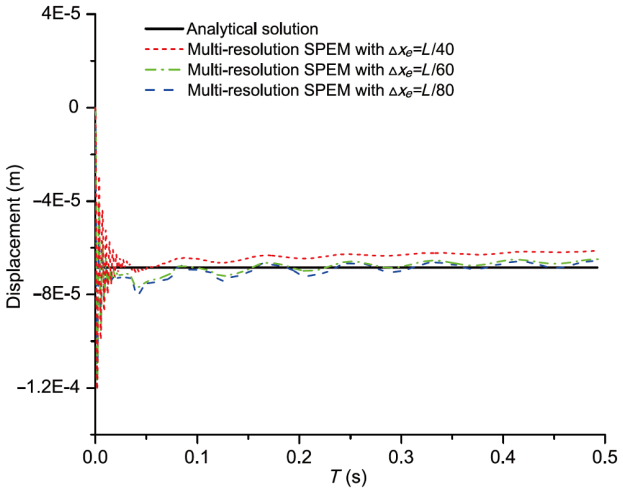

Figure 8 (Color online) Comparison of midpoint displacements of elastic plate obtained from analytical solution and multi-resolution SPEM with different spatial resolutions (element leg lengths).

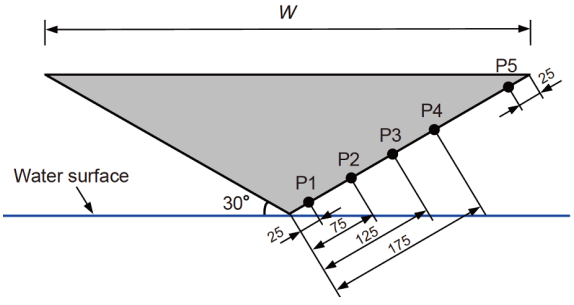

Figure 9 (Color online) Model set-up for the water entry of a wedge.

in the multi-resolution SPEM simulation and about 360000 elements in the simulation by the SPEM with a fine spatial resolution (no particle refinement). In this situation, the local spatial resolution near the wedge in multi-resolution SPEM is similar to that in the conventional SPEM with a fine resolution. Figure 11 shows the distributions of the particles and elements during the water entry process obtained using the multi-resolution SPEM. To ensure the stability of the

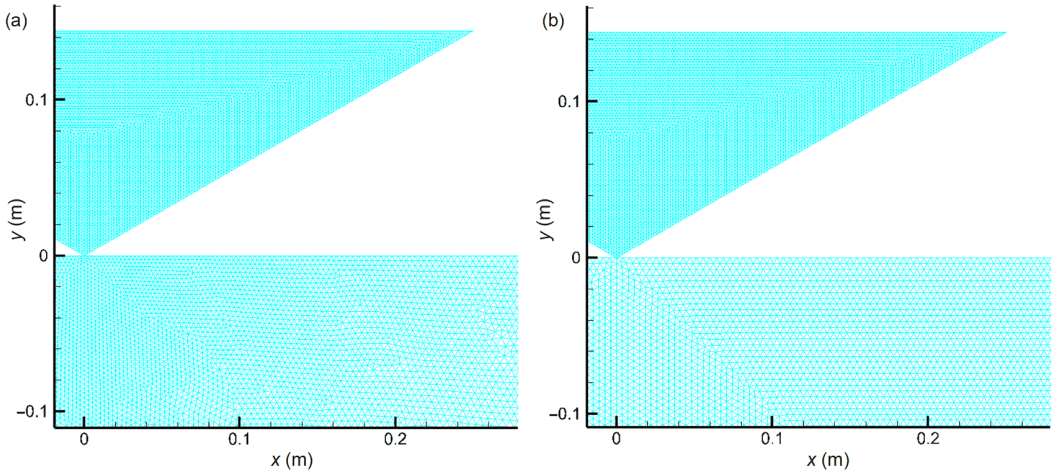

Figure 10 (Color online) Mesh distributions in (a) case I with variable mesh sizes and (b) case II with a fixed mesh size.

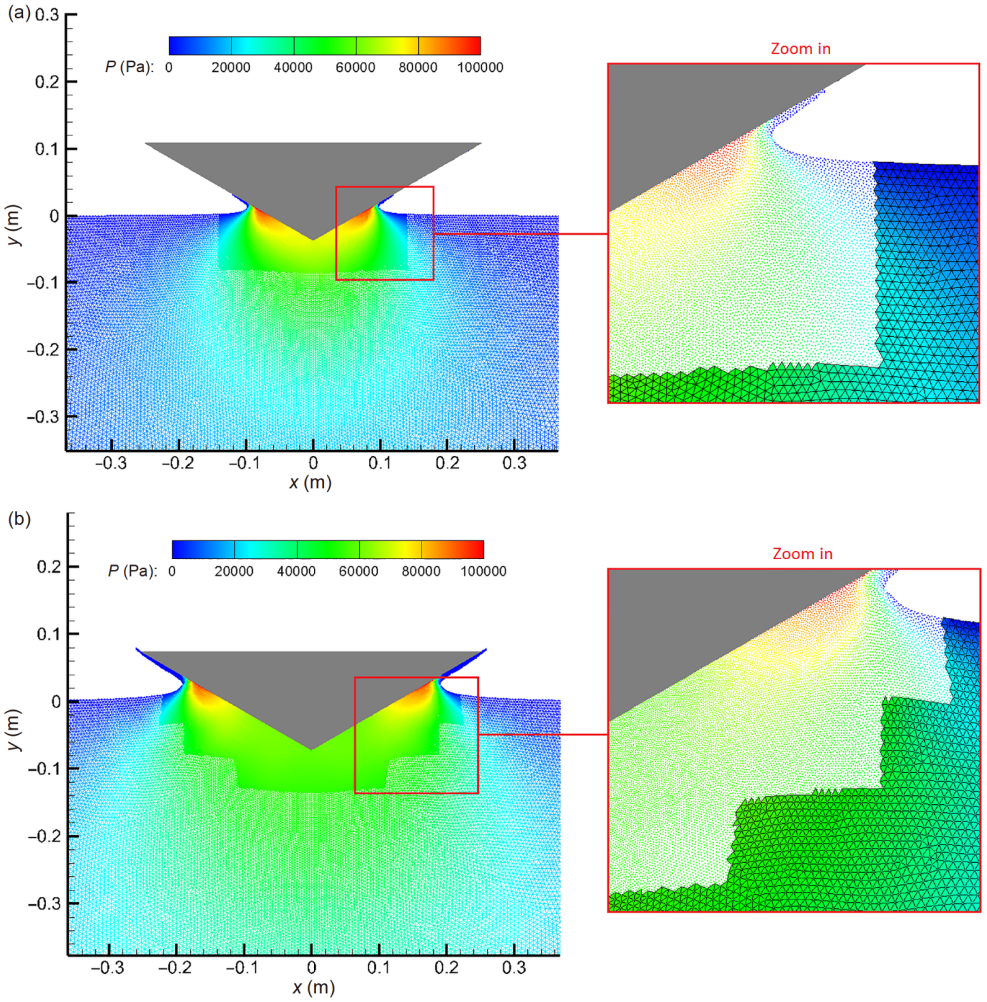

Figure 11 (Color online) Particle and element distributions obtained using the multi-resolution SPEM in case I at T = 0.006 s (a) and 0.012 s (b).

simulation and avoid the frequent evolution of the multi-resolution interfaces, we convert the elements in the region around the water entry point (0, 0) into refined particles before the simulation. During the water entry process, the multi-resolution element-particle interfaces change following the variation of the fluid-structure interfaces. A smooth pattern of the pressure is apparently obtained in the corresponding regions with refined particles and coarse elements, and the pressure distribution is continuous across the multi-resolution element-particle interfaces. Then, we compare the numerical results of the conventional SPEM with a fine spatial resolution and multi-resolution SPEM in Figure 12. This comparison shows the good agreement of the solutions of the two approaches, including the pressure field, wedge position, and free-surface shapes. Therefore, the implementation of multi-resolution technique in the SPEM can be quantitatively validated.

As shown in Figures 13 and 14, we perform some quantitative comparisons of the results obtained from different sources. As for the vertical force and vertical velocity of the

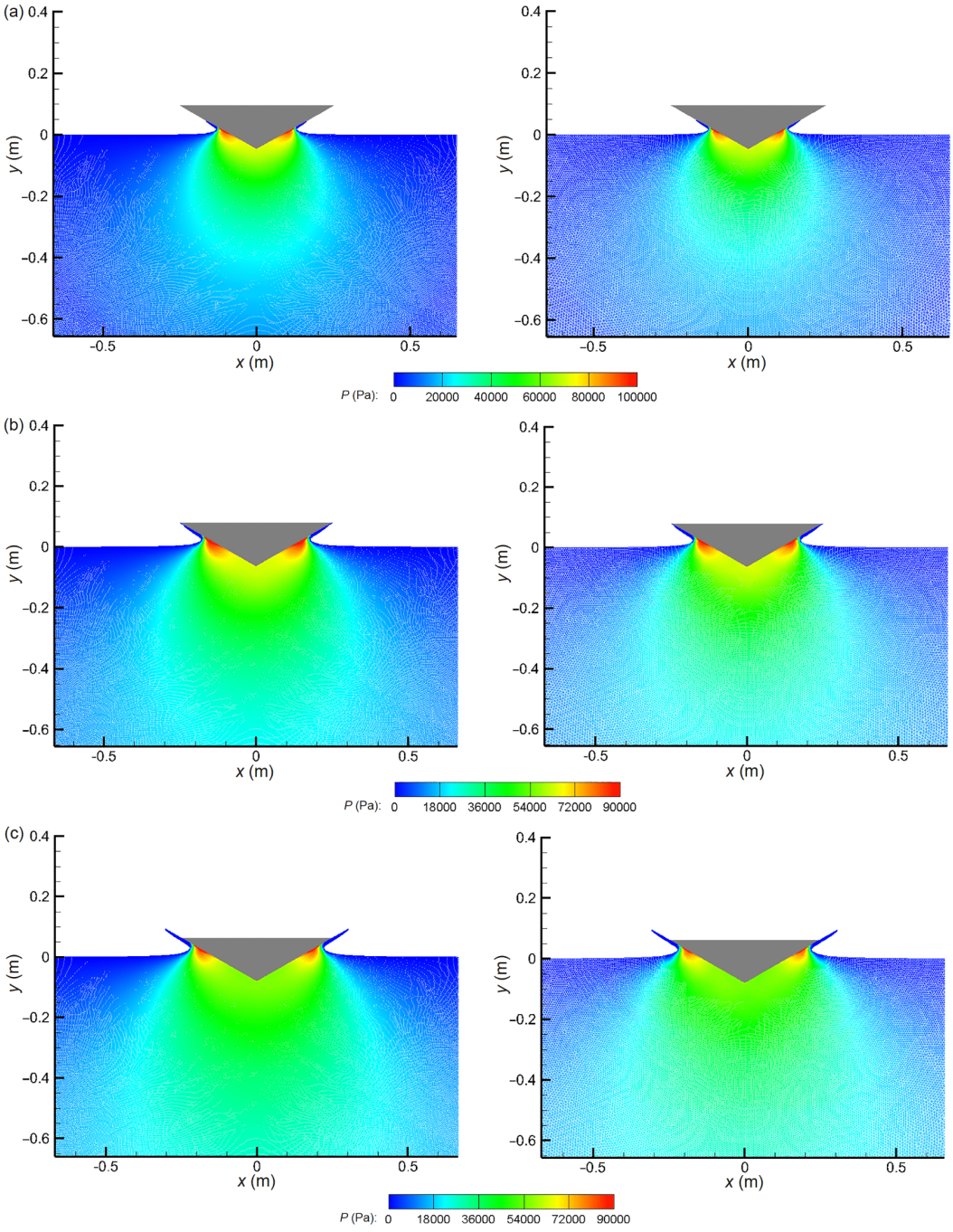

Figure 12 (Color online) Comparison of pressure fields during the water entry process obtained using the SPEM with a fine spatial resolution (left) and the multi-resolution SPEM (right), case I at T = 0.008, 0.011, and 0.014 s from (a) to (c).

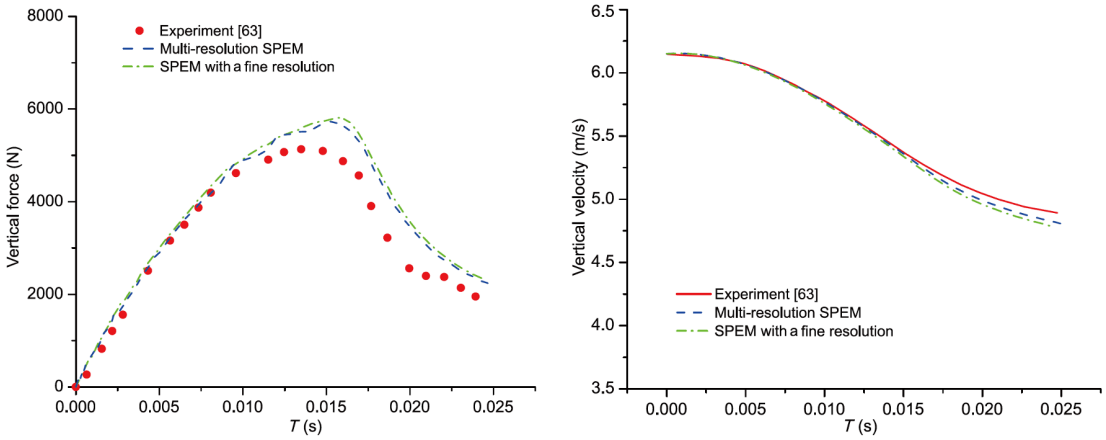

Figure 13 (Color online) (a) Vertical force and (b) vertical velocity of the wedge during the water entry process, case I.

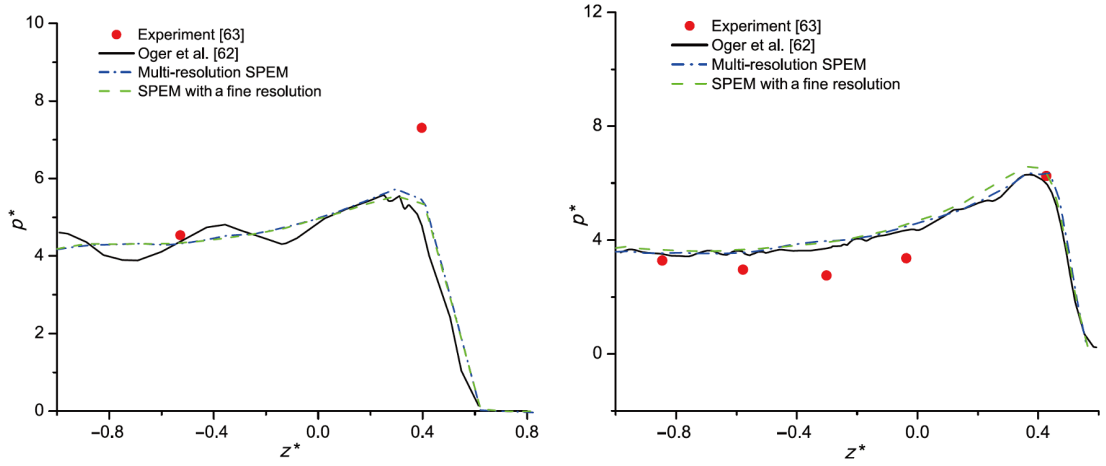

Figure 14 (Color online) Pressure distribution on the wedge (case I) at simulation time (a) T = 0.00435 s and (b) T = 0.0158 s, $p^* = P/0.5\rho_f V^2(t)$, $z^* = z/\int_0^t V(t)\mathrm{d}t$.

wedge during the water entry process, the conventional SPEM and multi-resolution SPEM can achieve results that are very close to the experimental observations [63]. The present numerical solutions overestimate the vertical force on the wedge, possibly because of the ignored 3D effects [62]. As for the pressure distribution on the wedge, the conventional SPEM with a fine resolution and the multi-resolution SPEM solutions agree well again with the reference results, except for the numerical results that show a slight deviation from the experimental data. In all the quantitative comparisons, the multi-resolution SPEM results are in a good agreement with the solutions by the conventional SPEM with a fine resolution. This result highlights the accuracy of the multi-resolution SPEM for modeling highly nonlinear problems involving free-surface flows.

The particle resolution around the water entry region in case I is much higher than that in case II. Hence, the particle-based modeling consumes more time than the element-based modeling in case I. As the numbers of the refined particles in the local regions of multi-resolution SPEM and conventional SPEM with a fine resolution are similar, the advantage of the multi-resolution SPEM in terms of efficiency is more evident for case II with a fixed mesh size than for case I. Furthermore, the SPEM consumes less time for simulating case II because more elements rather than particles are adopted in such a case if the total number of elements and particles is determined. Therefore, we utilize case II to test the efficiency of SPH, SPEM with a constant resolution, and multi-resolution SPEM (Table 1). These three approaches have similar spatial resolutions in the local region around the wedge. We observe that relative to the SPH method, the SPEM can greatly decrease the computational time because most of the fluid region is modeled using finite elements and only local fluid regions with moving interfaces or free surfaces are treated by particles. We should note that the conventional SPEM with a constant resolution and the multi-resolution SPEM use similar numbers of particles to model the local fluid region, whereas the multi-resolution SPEM

Table 1 Comparison of computational costs in the water entry case II with a fixed mesh size (computational domain: 3 m × 1.5 m)

Real time (s)	CPU time (min)		
	SPH with 540000 particles	SPEM with 540000 initial elements	Multi-resolution SPEM with 180000 initial elements
0.02	3828	255	132
0.025	4873	352	186

employs few elements for treating other fluid regions. Therefore, the multi-resolution SPEM does not hugely improve the efficiency of the conventional SPEM, and the time-consuming particle simulations with these two approaches are close to one another. Nevertheless, the multi-resolution SPEM is still much more efficient than the conventional SPEM with a constant resolution when the local spatial resolution is determined, as shown in Table 1. It is worth noting that significant computation cost is saved by the multi-resolution SPEM in comparison to SPH using a constant resolution because the number of particles in the SPEM simulation is very limited (around 10000) while most of the fluid region is modeled using coarse elements.

3.3 Water exit and entry of a cylinder

In this section, the water exit and entry of a cylinder are simulated by different approaches to demonstrate the superior efficiency of the multi-resolution SPEM. The model set-up for the present work is the same as that described in refs. [64,65], but a different computational domain size is adopted in the present simulation. In this problem, a cylinder with a diameter of 2.0 m is initially placed at d = 1.25 m below the static water surface. The gravitational acceleration is set as g = 1.0 m/s^2, and the cylinder has an impulsive upward velocity of V_0 = 0.39 m/s for the water exit problem (downward velocity in cylinder sinking case). We perform our present simulation with a time step of 2 × 10^{-5} s. The dimensionless time is taken as $T = |V_0 t / d|$, where t is the real time. The fluid domain is set with a length of 20 m and a depth of 11.25 m. Different from the water entry of the wedge in sect. 3.2 using nonuniform and uniform mesh systems, the computational domain is discretized by a uniform mesh system in this case.

Figures 15 and 16 illustrate the accuracy of the implementation of the multi-resolution technique in the SPEM. As shown in Figure 15, the water exit of a cylinder at different time instants is obtained from the reference solutions and the multi-resolution SPEM. We observe that the multi-resolution SPEM can effectively simulate the water exit process while producing free surfaces close to the numerical solutions in refs. [64,65]. These numerical results are slightly different from the theoretical results [66] as the nonlinear fluid dynamics (breaking thin fluid layer) make the theoretical results unreliable. This difference explains the theoretical solution being unavailable after T = 0.6.

As the computational domain is very large, it is not necessary to initially model the whole computational domain using finite elements for the sake of saving time. Therefore, a local square region around the cylinder (x = −1.8-1.8 m, y = −3.25-0 m) is preset with refined particles, and the frequent variations of the multi-resolution element-particle interfaces (like the water entry case) are avoided, as shown in Figure 16. It is noted that at the later stage of the water exit process, the multi-resolution element-particle interfaces are changed due to large deformations of the elements in a wide fluid domain. It also manifests that a continuous pressure distribution across the multi-resolution element-particle interfaces can be obtained by the present method.

As for modeling the sinking of a cylinder, we also preset refined particles in the local square region around the cylinder (x = −1.8-1.8 m, y = −3.1-0 m). In this case, the multi-resolution region changes with the sinking of the cylinder. Figure 17 shows the cylinder sinking process obtained from different approaches. The free-surface configurations produced by the multi-resolution SPEM agree well with those obtained from other numerical solutions. Furthermore, we show the multi-resolution element-particle interfaces during the cylinder sinking process in Figure 18. It is observed that a smoothed velocity field can be attained by the present method. This result highlights the effectiveness of the proposed algorithm in treating multi-resolution interfaces. By using the water exit and entry cases, we can effectively validate the accuracy of the multi-resolution SPEM in simulating FSIs with free-surface flows.

We compare the computational costs of the SPH simulations, conventional SPEM with a constant resolution, and multi-resolution SPEM, as shown in Table 2. The resolution in the refined region for the multi-resolution SPEM is the same as that for the conventional SPEM or SPH method with a constant resolution. It is seen that the SPEM significantly saves computational time relative to the SPH method as the major part of the fluid region is efficiently modeled by elements. An attractive result is that the multi-resolution SPEM can greatly improve the computational efficiency of the conventional SPEM when the spatial resolution of a target region is determined. That is to say, the simulation time of the multi-resolution SPEM may be several tenths of that of the SPH method with a constant resolution because only the local fluid region around the cylinder is modeled using refined particles while the large fluid domain is treated by coarse elements. This feature presents a huge improvement

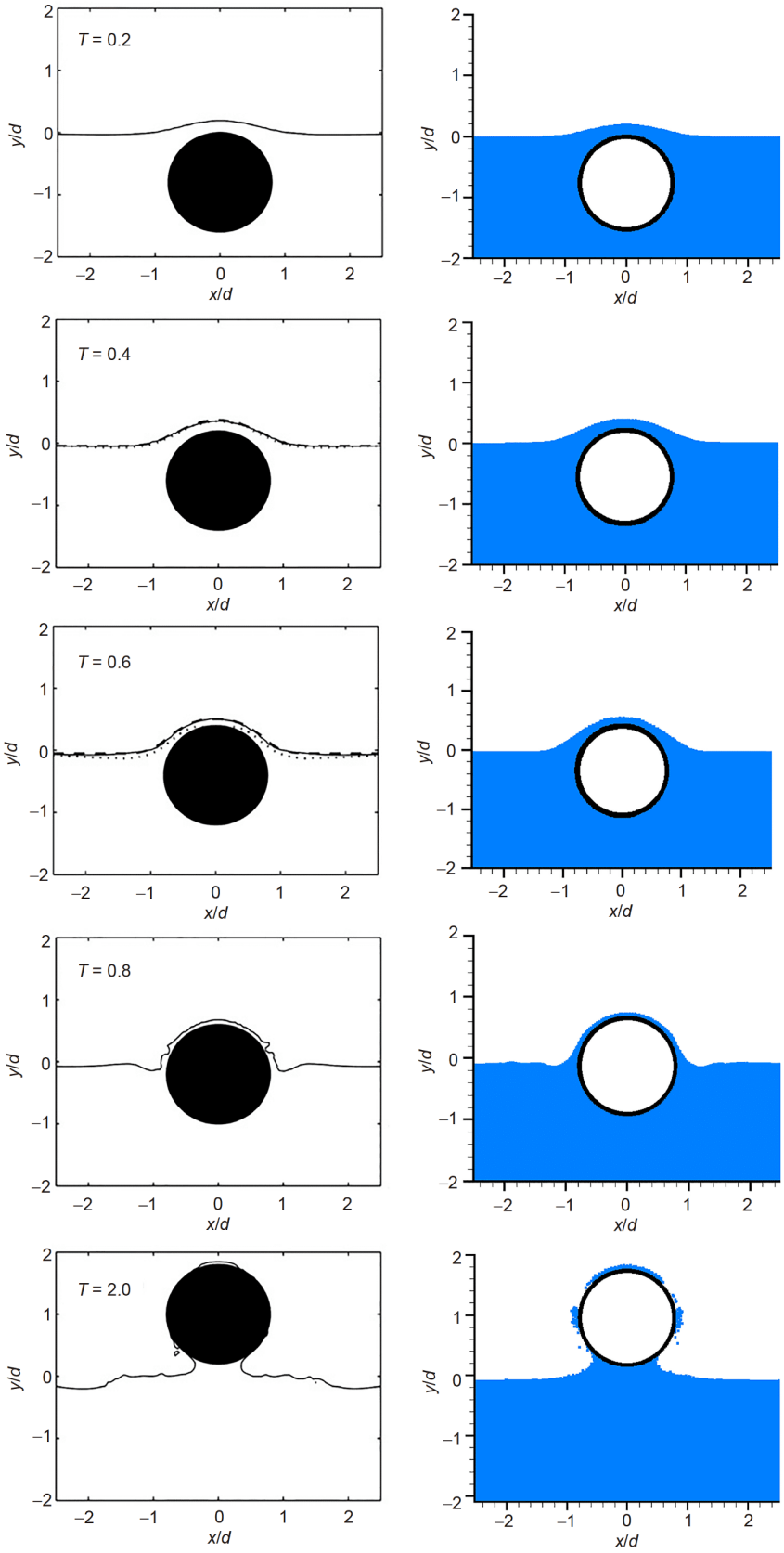

Figure 15 (Color online) Water exit of a cylinder at different time instants from the left: numerical results by Lin [65] (solid line), numerical results by Greenhow and Moyo [64] (dashed line), theoretical solutions by Tyvand and Miloh [66] (dotted line); and from the right: present multi-resolution SPEM. From up to down, T = 0.2, 0.4, 0.6, 0.8, and 2.0.

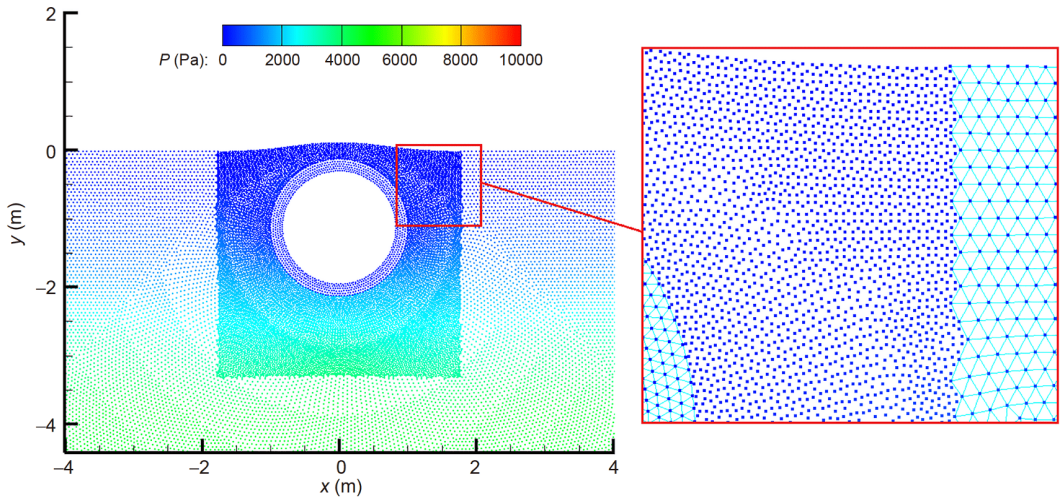

Figure 16 (Color online) Pressure field of the fluid and the enlarged view of the element-particle interface in the case of water exit, obtained using the multi-resolution SPEM at $T = 0.1$.

in efficiency over the conventional particle-based SPH method.

It should also be noticed that the efficiency improvement of the multi-resolution SPEM over the conventional SPEM is not as much as that in the water entry case (sect. 3.2). This difference is due to the large region with refined particles being preset in the water exit case. Moreover, the cylinder region is also larger than the wedge region. Consequently, particle-based modeling takes up a larger proportion in the water exit case, and the multi-resolution SPEM and conventional SPEM with a fine resolution consume a similar amount of time for this part of the computation. Actually, the efficiency improvement of the multi-resolution SPEM depends on the ratio of particle-based modeling to element-based modeling. If a large computation domain is handled by coarse elements and a smaller local region is treated using refined particles, then the multi-resolution SPEM can greatly reduce the computational time compared to the conventional SPEM with a fine resolution. By contrast, when a small computational domain is adopted or most of the fluid region undergoing large deformations is modeled using refined particles, the efficiency improvement of the multi-resolution SPEM is not so evident, just as shown in the dam breaking case (sect. 3.4).

3.4 Breaking dam flow on an elastic plate

Further, we model the case of breaking dam flow on an elastic plate to test the accuracy and efficiency of the multi-resolution SPEM. Figure 19 shows the model set-up for this example. A hydrostatic column is released from the left side of the container and then collides with the clamped elastic plate. The length of the container is set as $L = 0.584$ m. The width and height of the water column are $W = 0.146$ m and $H = 0.292$ m, respectively. An elastic plate is clamped on the middle bottom of the container and is set with a height of $h = 0.085$ m and width of $s = 0.012$ m. The density of the plate is specified as $\rho_s = 2500$ kg/m^3. A linear elasticity constitutive description is employed to model the elastic plate. The Poisson's ratio and Young's modulus of the plate are $\upsilon = 0$ and $E = 10^6$ Pa, respectively. These material parameters are the same as those adopted in ref. [67]; in this way, we can realize a good comparison with the reference results.

In this case, the fluid regions undergoing large deformations are adaptively modeled using refined particles. At a later stage of the simulation, most part of the fluid domains turns out to be refined particle regions as they all undergo large fluid deformations. Therefore, the multi-resolution SPEM does not show much improvement in terms of efficiency in this case. We adopt this example to mainly test the accuracy of the multi-resolution approach since the improved efficiency attained by our present method has been fully demonstrated in previously explained numerical examples.

Figure 20 shows the comparison of the pressure and stress fields between the simulation results of the multi-resolution SPEM and conventional SPEM with a fine resolution. Figure 21 presents the configurations of the free-surface and solid structure at two time instants of the simulations of the two approaches. The multi-resolution SPEM can produce numerical results very close to the SPEM with a fine resolution, including the pressure distribution in the fluid, stress distribution in the solid, free-surface shape, and baffle deformation during the dam breaking process. At the simulation time $T = 0.2$ s, the breaking free surface obtained by the multi-resolution SPEM is slightly higher than that produced by the SPEM with a fine resolution. Nevertheless, these comparisons qualitatively demonstrate the accuracy of the present multi-resolution technique introduced to the SPEM.

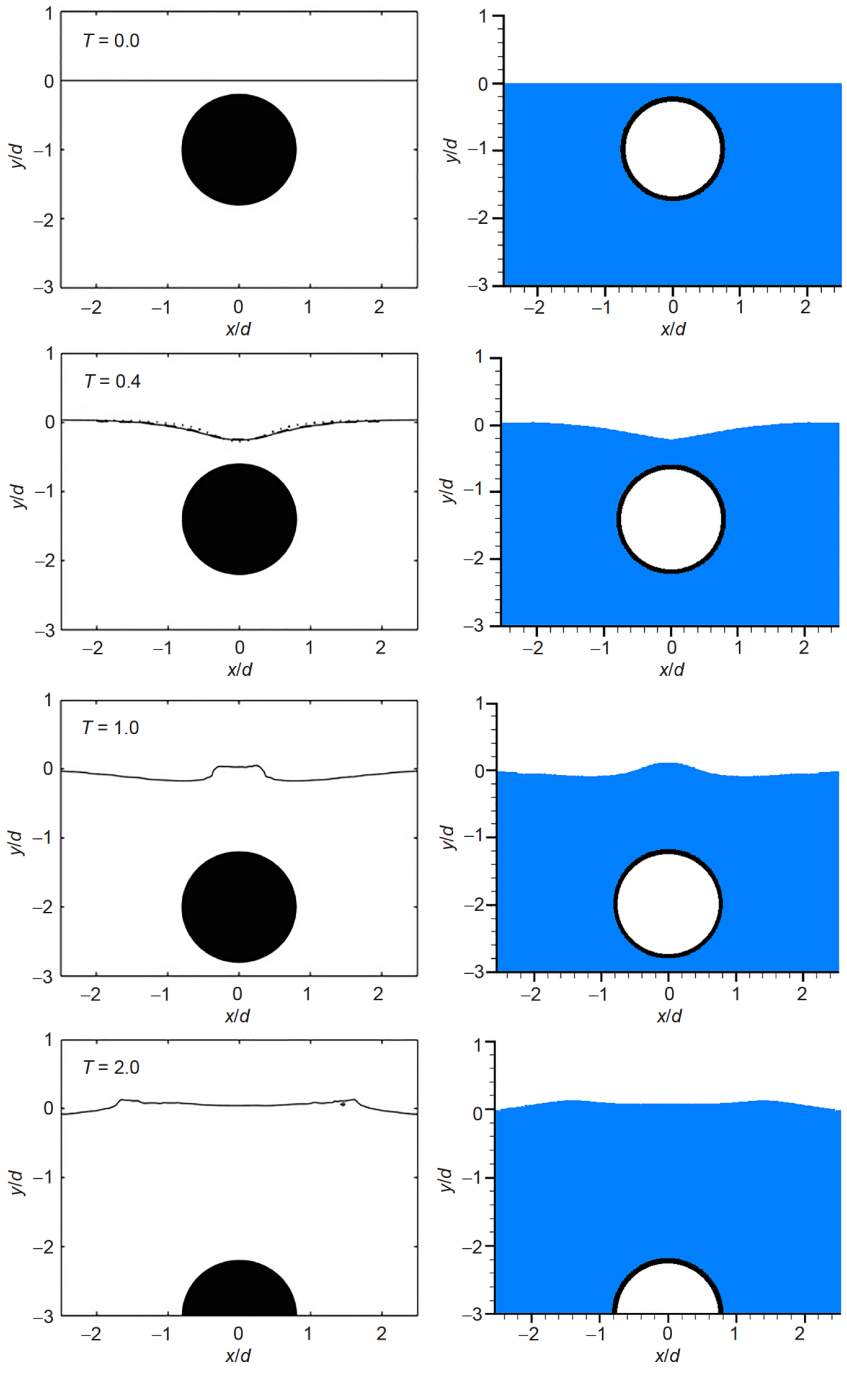

Figure 17 (Color online) Water entry of a cylinder at different time instants obtained from the left: numerical results by Lin [65] (solid line), numerical results by Greenhow and Moyo [64] (dashed line), theoretical solutions by Tyvand and Miloh [66] (dotted line); and from the right: present multi-resolution SPEM. From up to down, T = 0.0, 0.4, 1.0, and 2.0.

We should mention that in the dam breaking case, the pressure field of the fluid may not be smooth at the initial stage of the simulation because of the frequent variations of the multi-resolution element-particle interfaces. However, when more fluid regions undergoing large deformations have been converted into refined particles, the pressure distribution of the fluid obtained by the multi-resolution SPEM becomes relatively smooth, as shown in Figure 20. Although the pressure field may be influenced by the frequent changing of the multi-resolution interfaces, the multi-resolution SPEM can achieve quantitatively good results close to the reference data [67] (Figure 22). We also observe that compared with the simulation results by the conventional SPEM with a coarse resolution, the multi-resolution SPEM results agree more with the SPEM results with refined particles.

As mentioned previously, the enhanced efficiency of the

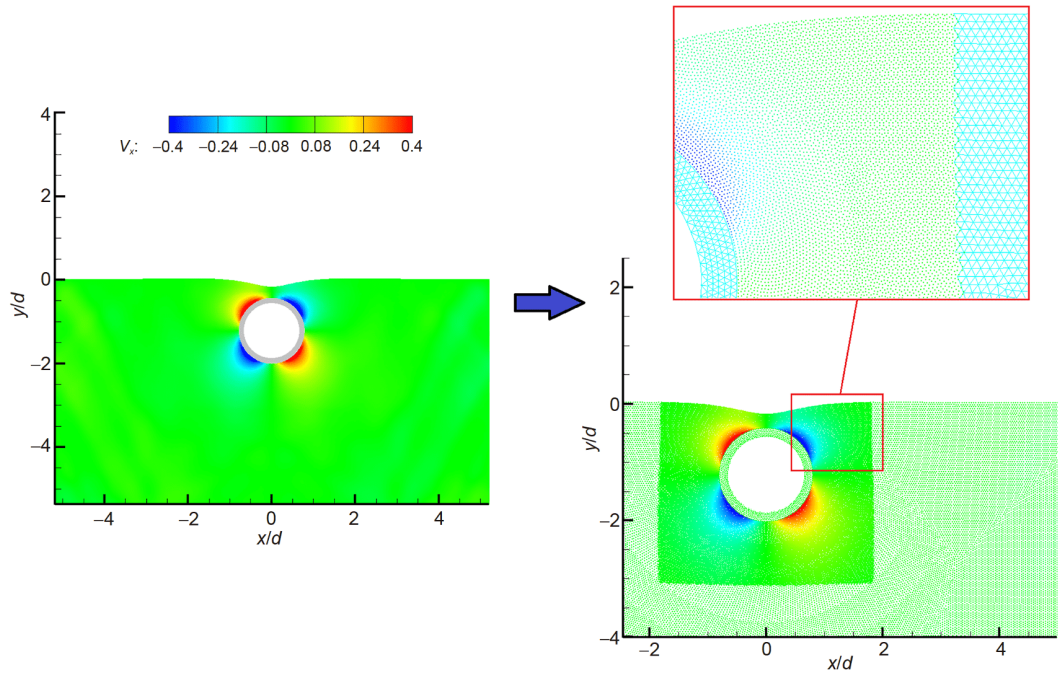

Figure 18 (Color online) Horizontal velocity field of the fluid and the zoomed-in view of the element-particle interface during the cylinder sinking process.

Table 2 Comparison of computational efforts in the water exit case[a)]

Real time t (s)	Refined particle resolution Δx (m)	CPU time (min)		
		SPH with 450000 particles	SPEM with 450000 initial elements	Multi-resolution SPEM with 150000 initial elements
1.0	0.022	3361	319	207
2.0	0.022	6806	647	415

a) Computational domain: 20 m × 11.25 m.

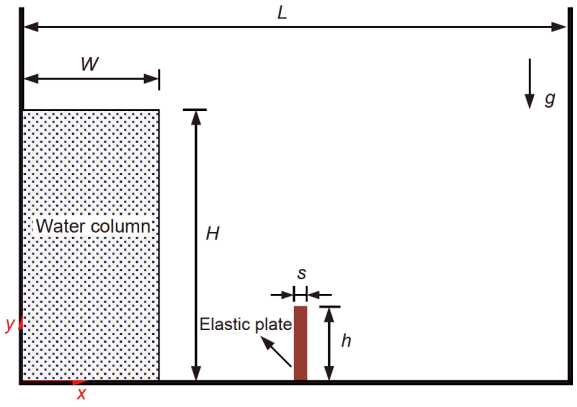

Figure 19 (Color online) Model set-up for the case of breaking dam flow on an elastic plate.

multi-resolution SPEM depends on the ratio of the particles to elements. Hence, the efficiency advantage of the multi-resolution SPEM over the conventional SPEM is not obvious in this case. Furthermore, the efficiency improvement of the conventional SPEM over the SPH method is not as evident as that observed in the previous cases because the computational domain is smaller, and most of the fluid region undergoes large deformations and is modeled using particles in this case. Nevertheless, we still show the comparisons of the computational costs of these approaches, as listed in Table 3. In the case of the multi-resolution SPEM simulation, the resolution of the converted particles is the same as that for the other two cases, i.e., $\Delta x = 0.00075$ m. The FEM-SPH represents the coupling of the FEM with the SPH in which the entire fluid region is modeled using the SPH method, and the solid structure is treated by the FEM. For modeling such a case ($T = 0.15$ s), the computational time of the multi-resolution SPEM is 81% that of the conventional SPEM and 20% that of the FEM-SPH. In summary, the dam breaking case validates the accuracy of the multi-resolution SPEM and shows its efficiency advantage to some degree.

4 Conclusions

In this work, a multi-resolution technique is introduced to the

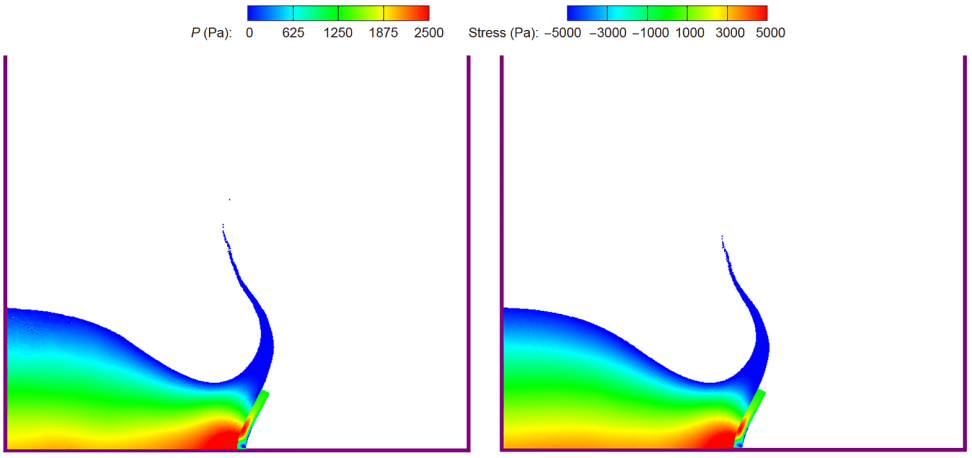

Figure 20 (Color online) Pressure distribution in fluid and stress field in the structure at T = 0.2 s obtained using (a) multi-resolution SPEM, and (b) conventional SPEM with a constant (fine) resolution.

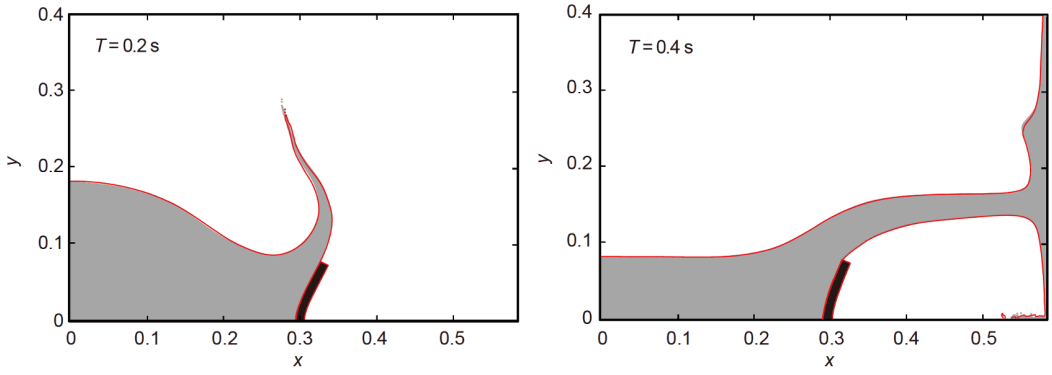

Figure 21 (Color online) Evolution of free-surface shape in the case of breaking dam flow on an elastic plate, obtained using multi-resolution SPEM (gray field) and conventional SPEM with a constant (fine) resolution (red line). (a) T = 0.2 s; (b) T = 0.4 s.

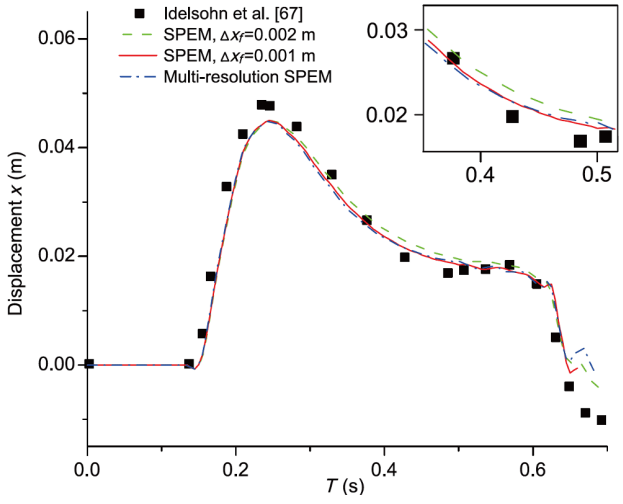

Figure 22 (Color online) Upper left corner's displacement of the elastic plate obtained from different sources. The present simulations are conducted with a solid element length Δx_s = 0.001 m. The initial fluid element length in the case of using the multi-resolution SPEM is Δx_f = 0.002 m.

recently developed SPEM. In the SPEM, both the fluid and solid regions are initially modeled using the S-FEM. During the simulation process, the fluid regions under large deformations are adaptively modeled using the improved SPH method, which is very effective in treating moving interfaces and free surfaces. Therefore, both the computational accuracy and efficiency can be enhanced by SPEM. Recently, multi-resolution simulations have become very popular in the field of CFD because this approach can greatly reduce the computational cost and well produce detailed information in local regions. In the present work, we introduce a multi-resolution technique for the SPEM and develop a novel algorithm to treat multi-resolution element-particle interfaces on the basis of splitting ghost particles. From various numerical examples, we demonstrate the following:

The present multi-resolution SPEM can treat moving multi-resolution regions with arbitrary shapes along with evolving FSI interfaces.

The developed multi-resolution element-particle coupling algorithm can accurately transfer information between coarse fluid elements and refined fluid particles.

The virtual particle coupling strategy can effectively treat FSI interfaces with different spatial resolutions in fluids and

Table 3 Comparison of computational efforts for real time of 0.25 s in case of dam breaking through an elastic plate

Real time (s)	Refined particle resolution Δx (m)	CPU time (s)		
		FEM-SPH with refined resolution	SPEM with refined resolution	Multi-resolution SPEM
0.15	0.00075	22699	5711	4643
0.25	0.00075	36862	19320	16554

structures.

The multi-resolution SPEM can greatly reduce the computational cost relative to the SPH method, and it is more efficient than the conventional SPEM with a constant resolution.

The multi-resolution SPEM shows a good convergent performance for modeling fluid-elastic structure interaction problems, and the multi-resolution SPEM results match very well with those obtained by the conventional SPEM with a fine resolution.

The multi-resolution SPEM can be further integrated with some advanced adaptive mesh refinement techniques. For instance, the dynamic mesh refinement may be performed on the element region of the SPEM, and the refined element region may be adaptively converted into particles to accurately model the regions of interest. Besides, multiphase simulations using the SPH method are time consuming because of the required small time step. The multi-resolution SPEM can be an attractive approach to handle multiphase problems due to its relatively high efficiency.

This work was supported by the National Numerical Wind Tunnel Project (Grant No. NNW2019ZT2-B02), the National Natural Science Foundation of China (Grant Nos. 12032002, 51779003, and 11902005) and the Sino-German Mobility Programme (Grant No. M-0210). The authors appreciate the help from Dr. Muhammad Saif Ullah Khalid for smoothing the paper and giving constructive suggestions.

1 Z. L. Zhang, T. Long, J. Z. Chang, and M. B. Liu, Comput. Methods Appl. Mech. Eng. **356**, 261 (2019).
2 S. R. Idelsohn, E. Oñate, and F. D. Pin, Int. J. Numer. Meth. Engng. **61**, 964 (2004).
3 S. Meduri, M. Cremonesi, U. Perego, O. Bettinotti, A. Kurkchubasche, and V. Oancea, Int. J. Numer. Meth. Engng **113**, 43 (2017).
4 M. L. Cerquaglia, D. Thomas, R. Boman, V. Terrapon, and J. P. Ponthot, Comput. Methods Appl. Mech. Eng. **348**, 409 (2019).
5 A. Franci, and M. Cremonesi, Comp. Part. Mech. **4**, 331 (2017).
6 J. R. Cho, and H. W. Lee, Comput. Methods Appl. Mech. Eng. **193**, 2581 (2004).
7 J. Kim, D. Kim, and H. Choi, J. Comput. Phys. **171**, 132 (2001).
8 E. A. Fadlun, R. Verzicco, P. Orlandi, and J. Mohd-Yusof, J. Comput. Phys. **161**, 35 (2000).
9 C. W. Hirt, and B. D. Nichols, J. Comput. Phys. **39**, 201 (1981).
10 D. Peng, B. Merriman, S. Osher, H. Zhao, and M. Kang, J. Comput. Phys. **155**, 410 (1999).
11 P. P. Wang, Z. F. Meng, A. M. Zhang, F. R. Ming, and P. N. Sun, Comput. Methods Appl. Mech. Eng. **357**, 112580 (2019).
12 X. Zheng, R. Chen, M. Luo, E. Kazemi, and X. Liu, J. Mt. Sci. **16**, 1913 (2019).
13 C. Tsurudome, D. Liang, Y. Shimizu, A. Khayyer, and H. Gotoh, J. Hydrodyn. **32**, 664 (2020).
14 X. F. Yang, and M. B. Liu, Sci. China-Phys. Mech. Astron. **56**, 315 (2013).
15 M. Rezavand, C. Zhang, and X. Hu, J. Comput. Phys. **402**, 109092 (2019), arXiv: 1903.09216.
16 B. X. Zheng, L. Sun, and P. Yu, J. Comput. Phys. **431**, 110119 (2021).
17 X. Yang, and S. C. Kong, Comput. Phys. Commun. **239**, 112 (2019), arXiv: 1808.02028.
18 K. Szewc, J. Pozorski, and A. Tanière, Int. J. Heat Mass Transfer **54**, 4807 (2011).
19 F. Garoosi, and A. Shakibaeinia, Int. J. Heat Mass Transfer **150**, 119377 (2020).
20 P. Yang, C. Huang, Z. Zhang, T. Long, and M. Liu, Int. J. Heat Mass Transfer **166**, 120758 (2021).
21 Z. L. Zhang, and M. B. Liu, J. Manuf. Proc. **41**, 208 (2019).
22 M. B. Liu, Z. L. Zhang, and D. L. Feng, Comput. Mech. **60**, 513 (2017).
23 M. B. Liu, and G. R. Liu, Arch. Comput. Methods Eng. **17**, 25 (2010).
24 J. J. Monaghan, Annu. Rev. Fluid Mech. **44**, 323 (2012).
25 R. Vacondio, C. Altomare, M. De Leffe, X. Hu, D. Le Touzé, S. Lind, J. Marongiu, S. Marrone, B. D. Rogers, and A. Souto-Iglesias, Comput. Part. Mech. **21**, https://doi.org/10.1007/s40571-40020-00354-40571
26 G. Fourey, G. Oger, D. Touzé, and B. Alessandrini, in *IOP Conference Series: Materials Science and Engineering* (IOP Publishing, Bristol, 2010), p. 012041.
27 D. Hu, T. Long, Y. Xiao, X. Han, and Y. Gu, Comput. Methods Appl. Mech. Eng. **276**, 266 (2014).
28 C. Hermange, G. Oger, Y. Le Chenadec, and D. Le Touzé, Comput. Methods Appl. Mech. Eng. **355**, 558 (2019).
29 Z. L. Zhang, M. S. U. Khalid, T. Long, J. Z. Chang, and M. B. Liu, J. Fluids Struct. **94**, 102942 (2020).
30 S. Marrone, A. Di Mascio, and D. Le Touzé, J. Comput. Phys. **310**, 161 (2016).
31 L. Chiron, S. Marrone, A. Di Mascio, and D. Le Touzé, J. Comput. Phys. **364**, 111 (2018).
32 C. Huang, T. Long, and M. B. Liu, Int. J. Numer. Meth. Fluids **90**, 564 (2019).
33 M. J. Berger, and P. Colella, J. Comput. Phys. **82**, 64 (1989).
34 M. Vanella, P. Rabenold, and E. Balaras, J. Comput. Phys. **229**, 6427 (2010).
35 R. Vacondio, B. D. Rogers, P. K. Stansby, P. Mignosa, and J. Feldman, Comput. Methods Appl. Mech. Eng. **256**, 132 (2013).
36 D. A. Barcarolo, D. Le Touzé, G. Oger, and F. de Vuyst, J. Comput. Phys. **273**, 640 (2014).
37 R. Vacondio, B. D. Rogers, and P. K. Stansby, Int. J. Numer. Meth. Fluids **69**, 1377 (2012).
38 L. Chiron, G. Oger, M. de Leffe, and D. Le Touzé, J. Comput. Phys. **354**, 552 (2018).
39 P. N. Sun, D. Le Touzé, and A. M. Zhang, Eng. Anal. Bound. Elem. **104**, 240 (2019).
40 J. Feldman, and J. Bonet, Int. J. Numer. Meth. Eng. **72**, 295 (2007).
41 Y. R. López, D. Roose, and C. Recarey Morfa, Comput. Mech. **51**, 731 (2013).
42 R. Vacondio, B. D. Rogers, P. K. Stansby, and P. Mignosa, Adv. Water Resour. **58**, 10 (2013).
43 G. R. Liu, K. Y. Dai, and T. T. Nguyen, Comput. Mech. **39**, 859 (2007).
44 S. Marrone, A. Colagrossi, A. Di Mascio, and D. Le Touzé, J. Fluids Struct. **54**, 802 (2015).

45 P. N. Sun, M. Luo, D. Le Touzé, and A. M. Zhang, Phys. Fluids **31**, 117108 (2019).
46 S. Koshizuka, and Y. Oka, Nucl. Sci. Eng. **123**, 421 (1996).
47 S. Koshizuka, A. Nobe, and Y. Oka, Int. J. Numer. Meth. Fluids **26**, 751 (1998).
48 S. Shao, and E. Y. M. Lo, Adv. Water Resour. **26**, 787 (2003).
49 A. Khayyer, H. Gotoh, Y. Shimizu, K. Gotoh, H. Falahaty, and S. Shao, Coast. Eng. **140**, 1 (2018).
50 D. Wang, and P. L. F. Liu, Coast. Eng. **157**, 103657 (2020).
51 M. B. Liu, W. P. Xie, and G. R. Liu, Appl. Math. Model. **29**, 1252 (2005).
52 F. He, H. Zhang, C. Huang, and M. Liu, Coast. Eng. **156**, 103617 (2019).
53 D. Chen, W. Huang, and S. W. Sloan, Comput. Methods Appl. Mech. Eng. **343**, 490 (2019).
54 R. Xu, P. Stansby, and D. Laurence, J. Comput. Phys. **228**, 6703 (2009).
55 S. J. Lind, R. Xu, P. K. Stansby, and B. D. Rogers, J. Comput. Phys. **231**, 1499 (2012).
56 Y. Xiao, X. Han, and D. A. Hu, Comput. Mater. Con. **584**, 1 (2011).
57 T. Long, D. Hu, D. Wan, C. Zhuang, and G. Yang, J. Comput. Phys. **350**, 166 (2017).
58 X. Cui, G. R. Liu, G. Y. Li, G. Zhang, and G. Zheng, Comput. Mech. **45**, 141 (2010).
59 W. Zeng, and G. R. Liu, Arch. Comput. Methods Eng. **25**, 397 (2018).
60 Y. P. Zhao, Arch. Appl. Mech. **68**, 524 (1998).
61 M. Liu, and Z. Zhang, Sci. China-Phys. Mech. Astron. **62**, 984701 (2019).
62 G. Oger, M. Doring, B. Alessandrini, and P. Ferrant, J. Comput. Phys. **213**, 803 (2006).
63 R. Zhao, O. Faltinsen, and J. Aarsnes, in *Proceedings of the 21st Symposium on Naval Hydrodynamics* (Trondheim, 1997).
64 M. Greenhow, and S. Moyo, Philos. Trans. R. Soc. London. Ser. A-Math. Phys. Eng. Sci. **355**, 551 (1997).
65 P. Lin, Comput. Fluids **36**, 549 (2007).
66 P. A. Tyvand, and T. Miloh, J. Fluid Mech. **286**, 67 (1995).
67 S. R. Idelsohn, J. Marti, A. Limache, and E. Oñate, Comput. Methods Appl. Mech. Eng. **197**, 1762 (2008).